



저작자표시-비영리-변경금지 2.0 대한민국

이용자는 아래의 조건을 따르는 경우에 한하여 자유롭게

- 이 저작물을 복제, 배포, 전송, 전시, 공연 및 방송할 수 있습니다.

다음과 같은 조건을 따라야 합니다:



저작자표시. 귀하는 원저작자를 표시하여야 합니다.



비영리. 귀하는 이 저작물을 영리 목적으로 이용할 수 없습니다.



변경금지. 귀하는 이 저작물을 개작, 변형 또는 가공할 수 없습니다.

- 귀하는, 이 저작물의 재이용이나 배포의 경우, 이 저작물에 적용된 이용허락조건을 명확하게 나타내어야 합니다.
- 저작권자로부터 별도의 허가를 받으면 이러한 조건들은 적용되지 않습니다.

저작권법에 따른 이용자의 권리는 위의 내용에 의하여 영향을 받지 않습니다.

이것은 [이용허락규약\(Legal Code\)](#)을 이해하기 쉽게 요약한 것입니다.

[Disclaimer](#)

이학박사학위논문

**Anomalous and planar Hall effect
measurements of freely suspended
GaMnAs epilayers**

자가현수된 GaMnAs 에서의
비정상 홀 효과 와 평면 홀 효과 연구

2017 년 2 월

서울대학교 대학원

물리천문학부

이 재 현

**Anomalous and planar Hall effect
measurements of freely suspended
GaMnAs epilayers**

Jae-Hyun Lee

Supervised by

Professor Yun Daniel Park

A dissertation submitted to the faculty of
Seoul National University in partial fulfillment of the requirements
for the degree of doctor of philosophy

February 2017

Graduate school of department of Physics and Astronomy
Seoul National University

© Copyright by Jae-Hyun Lee, 2017

All rights reserved.

Abstract

Strain, a deformation representing the relative displacement between particles in a material body, has emerged as a novel parameter in spin-based physical phenomena. In GaMnAs thin film, magnetic anisotropy of the film is strongly influenced by strain built-in during pseudomorphic growth. In order to investigate strain-induced magnetic anisotropy changes as well as magnetic anisotropy at strain-free state, GaMnAs/GaAs/AlGaAs/GaAs structure was grown using UHV-MBE growth, with concentration of Mn ~6% and Al ~ 75%. Freely-suspended GaMnAs structures were fabricated using standard e-beam lithography, with aid of soft metallic electric leads. Freely-suspended structures were in van der Pauw and Hall bar geometry and each sample consist of a freely-suspended structure and a control structure. From temperature dependent longitudinal resistivity, no signs of changes in macroscopic properties nor possible damage during fabrication was observed. From anomalous Hall measurement of van der Pauw structure, in-plane-like magnetic anisotropy of GaMnAs under compressive strain has been modified to more-out-of-plane-like magnetic anisotropy. Further investigation was conducted in anomalous and planar Hall measurement of Hall bar structure. From angle dependent longitudinal and transverse Hall resistance, in-plane magnetic anisotropy from built-in compressive strain is greatly reduced in freely-suspended structures. Utilizing Stoner-Wohlfarth model and non-linear fitting, ratio between in-plane cubic anisotropy and uniaxial anisotropy in freely-suspended structure was estimated to be reduced by 24%. This manipulation of magnetic

anisotropy by nano-machining-based strain manipulation suggest possibility of dynamic strain manipulation via nano-machining technique.

Keywords: Diluted magnetic semiconductor, GaMnAs, Molecular beam epitaxy, Anomalous Hall effect, Planar Hall effect, Freely suspended, Magnetic anisotropy, Strain

Student ID: 2008-20446

Table of Contents

1	Introduction	1
1.1	Spintronics and emerge of diluted magnetic semiconductor	1
1.2	Strain: from an obstacle to a novel parameter in solid state physics.....	2
1.3	Motivation of this research	4
2	Theoretical background.	9
2.1	Ferromagnetism in GaMnAs.....	9
2.2	Magnetoresistance behavior in GaMnAs	12
2.2.1	Anomalous Hall Effect in GaMnAs	18
2.2.2	Stoner-Wohlfarth model	22
2.2.3	Shape anisotropy and strain-based anisotropy	25
2.2.4	Modification of Stoner-Wohlfarth for GaMnAs under compressive strain ..	32
3	Sample Preparation	37
3.1	MBE-growth of LT-GaMnAs/LT-GaAs/AlGaAs/GaAs structure	37
3.1.1	Introduction of MBE growth.....	37
3.1.2	Growth of LT-GaMnAs/LT-GaAs/AlGaAs/GaAs.....	41
3.2	Characterization of LT-GaMnAs/LT-GaAs/AlGaAs/GaAs	45

3.2.1	Post-Annealing.....	45
3.2.2	Determination of Mn and Al concentration	46
3.3	Fabrication of freely-suspended GaMnAs structures.....	49
3.3.1	Motivation of freely-suspended structure	49
3.3.2	Overview of the fabrication process	52
3.3.3	Fabrication : electrode-deposition-first method.....	53
3.3.4	Fabrication : structure-definition-first method.....	56
4	Anomalous Hall effect measurements in freely-suspended GaMnAs microsheet in van der Pauw geometry	59
4.1	Sample preparation and measurement set-up.....	59
4.2	Temperature dependent longitudinal resistivity.....	60
4.3	Finite-element analysis of GaMnAs microsheet.....	62
4.4	Magnetoresistance measurement in freely-suspended GaMnAs microsheets. .	64
4.5	Summary	67
5	Anomalous and Planar Hall effect measurements in freely-suspended GaMnAs in Hall bar geometry	69
5.1	Sample preparation and measurement set-up.....	69
5.2	Finite-element analysis of GaMnAs Hall bar structure.....	70

5.3	Angle definition for planar and normal Hall geometry.....	72
5.4	Temperature dependent longitudinal resistivity.....	74
5.5	Planar Hall effect measurement of GaMnAs Hall Bar structure.....	76
5.6	Anomalous Hall effect measurement of GaMnAs Hall Bar structure	85
5.7	Estimation of anisotropy constant.....	89
6	Conclusion and Prospect.....	93
	Bibliography	97
	국문 초록.....	105

(Blank page)

List of figures

Figure 2.1 Lattice of GaMnAs with possible defects.....	11
Figure 2.2 Splitting of the isolated Mn acceptor level and splitting of the top of valence band in many-Mn system due to p - d hybridization	11
Figure 2.3 Schematic of magnetoresistance with perpendicular magnetization and parallel magnetization.....	13
Figure 2.4 A typical plot of resistance vs. applied magnetic field in the Co/Cu	13
Figure 2.5 The in-plane anisotropic magnetoresistance for the as-grown $\text{Ga}_{1-x}\text{Mn}_x\text{As}$ thin film.....	17
Figure 2.6 Schematic illustration of the Hall effect and the anomalous Hall effect	21
Figure 2.7 Illustration of the three main mechanism of anomalous Hall effect.....	21
Figure 2.8 Single domain hysteresis loop obtained for an arbitrary angle between the magnetic field and the anisotropy axis.....	24
Figure 2.9 Shape anisotropy in a prolate spheroid of Co	26
Figure 2.10 Shape anisotropy constant in prolate spheroid and demagnetization factor for different shapes	26
Figure 2.11 Schematics representing unstrained and deformed lattice and corresponding band structure changes.	28
Figure 2.12 Energy differences among different magnetization orientations versus in-plane strain.....	31
Figure 2.13 Hall resistance at various temperature for $\text{Ga}_{0.95}\text{Mn}_{0.05}\text{As}/\text{GaAs}$ and $\text{Ga}_{0.957}\text{Mn}_{0.043}\text{As}/(\text{In,Ga})\text{As}$	31

Figure 2.14 Energy landscape at zero field estimated from biaxial and uniaxial, and evolution of energy surface with increasing field	35
Figure 3.1 Schematics of typical MBE system	40
Figure 3.2 Mechanism of RHEED specular spot oscillation during growth.....	40
Figure 3.3 Schematics of structures and corresponding RHEED images	44
Figure 3.4 GaMnAs phase diagram	44
Figure 3.5 Resistance vs. temperature plot for different post-annealing temperatures....	48
Figure 3.6 High resolution HR-XRD θ - 2θ scan of sample	48
Figure 3.7 SEM image of GaMnAs Hall bar structure after sacrificial layer etch, non-contact optical profiler image of buckled Hall bar, and cross-sectional morphology extracted from optical profiler image.....	51
Figure 3.8 GaMnAs cross-like structures before and after sacrificial layer etch.	51
Figure 3.9 Schematics of fabrication processes	57
Figure 4.1 SEM image of control and free-standing van der Pauw structures.....	61
Figure 4.2 Temperature-dependent resistivity (ρ_{xx} vs. T) and the corresponding differential resistivity ($d\rho_{xx}/dT$).....	61
Figure 4.3 Finite-element analysis mapping the calculated stress distributions for the control and free-standing GaMnAs microsheets for $T = 300$ K and 10 K.....	63
Figure 4.4 . Longitudinal Hall resistance as a function of the applied magnetic field (ΔR_{xx} vs. H) at $T = 10$ K and transverse Hall resistance as a function of the applied magnetic field (R_{xy} vs. H) at $T = 10$ K, and Field-dependent transverse Hall resistance (R_{xy} vs. H) at various temperatures	66

Figure 5.1 SEM image of freely-suspended GaMnAs Hall bar structure	71
Figure 5.2 Non-contact optical profile image of suspended GaMnAs Hall bar structure	71
Figure 5.3 Finite-element analysis mapping the calculated stress distributions for the control and free-standing GaMnAs microsheets for $T = 300$ K and 10 K.....	73
Figure 5.4 Schematic for angle definition for planar Hall geometry.	73
Figure 5.5 Schematic for definition for angle definition for normal Hall geometry.....	73
Figure 5.6 Temperature-dependent resistivity (ρ_{xx} vs. T).....	75
Figure 5.7 Longitudinal resistance as a function of applied field angle (R_{xx} vs. θ) at the temperature of 4 K, 15 K, 30 K, 60 K, and 90 K.	78
Figure 5.8 Polar plot of longitudinal resistance as a function of applied field angle (R_{xx} vs. θ) at the temperature of 4 K, 15 K, 30 K, 60 K, and 90 K.	79
Figure 5.9 Transverse resistance as a function of applied field angle (R_{xx} vs. θ) at the temperature of 15 K and applied field of 200 Oe, 500 Oe, 1500 Oe and 12000 Oe.	81
Figure 5.10 Polar plot of transverse resistance as a function of applied field angle (R_{xx} vs. θ) at the temperature of 15 K and applied field of 200 Oe, 500 Oe, 1500 Oe and 12000 Oe.....	82
Figure 5.11 Longitudinal and transverse Hall resistance as a function of applied field (R_{xx} vs. H , R_{xy} vs. H) at the temperature of 4 K.....	87
Figure 5.12 Angle-dependent longitudinal resistance of GaMnAs structure.....	88
Figure 5.13 Magnetization angle as a function of applied magnetic field angle for suspended and unsuspended.	91

Figure 5.14 Sine value of magnetization phase lag as a function of magnetization angle for suspended and unsuspended.....	91
Figure 5.15 Estimated values of anisotropic constants	92

1 Introduction

1.1 Spintronics and emerge of diluted magnetic semiconductor

Spintronics, a study for manipulation of spin-based physical phenomena based on electronics emerged from the metallic materials such as Co, NiFe and has expanded its area into semiconductor. Spin-based physical phenomena such as giant magnetoresistance (GMR) and tunneling magnetoresistance (TMR) in metallic materials have been employed to various device application including magnetic read/write head in hard drive, magnetic random access memory (MRAM) and magnetic sensors [1]. Furthermore, recent studies have expanded application of spintronics to wide range varying from tunneling junction[2], domain wall[3] and even to organic spintronics [4].

Semiconductor spintronics, initiated by the proposal of Datta and Das [5], is an attempt to expand spin-based physical phenomena in metallic material to semiconductor material, utilizing both the spin degrees of freedom and the charge of carrier from dopant which are inherited from metal and semiconductor, respectively. Addition of spin degrees of freedom to a semiconductor system, described as spin field-effect transistor by early researchers, suggested possibility of low-power

consuming, highly-efficient electronic devices and has been expected to provide solution to critical issues in next generation devices [6].

.Among numerous candidates for semiconductor spintronics, diluted magnetic semiconductor (DMS), which exhibits both ferromagnetism and semiconductor properties, has drawn attention of many researchers in a wide range from group IV [7], II-VI [8], III-V [9] and even wide bandgap semiconductor and oxide [10]. Especially, III-Mn-V ferromagnetic semiconductors were intensively studied since first observation of ferromagnetic ordering in InAs and GaAs-based DMS due to advantages of Mn doping which serve as a dual role of local ferromagnetic moment and acceptor. III-V semiconductor, represented by III-As compound such as GaAs and InAs, has been widely studied for electronic device application as well as electron-based physical phenomena due to its outstanding electron mobility [11,12]. Incorporation of magnetic impurity, for instance Mn, into high mobility semiconductor allows utilization of both outstanding electrical properties of III-As semiconductor and ferromagnetic properties of magnetic material without further incorporation of carrier dopant.

1.2 Strain: from an obstacle to a novel parameter in solid state physics

Strain, a deformation representing the relative displacement between particles in a material body, has been treated as a significant obstacle in the process of thin

film growth [13]. Strain in the thin film usually originated from lattice-mismatch in the heteroepitaxial growth. When two materials with different lattice constant are grown onto each other, lattice-mismatch between two materials causes a deformation; material with larger lattice constant experience compressive strain and material with smaller lattice constant experience tensile strain. However, strain in a thin film usually accompanied by evolution of defects, dislocations or stacking faults. Furthermore, extreme level of strain ends up with the failure of the film, represented by crack. Therefore, ordinary strain in the thin film has been considered as the “to-be-removed’ obstacle in the growth of high-quality thin film and most of early works in strain engineering are mainly concentrated on reduction or evasion of strain in the thin film.

With rise of low dimensional material such as nanowires and quantum dots as well as functional structures like super-lattice, strain no longer considered as an obstacle, but an important factor of new possibility which may add a new functionality to materials. Strain-induced 3-D growth modes such as Stranski-Krastanov growth mode and Volmer-Weber growth mode were originally considered as the failure in thin film growth, but with emerge of nanowires, they have become a cornerstone for the growth of various nanostructures [14,15]. Strain engineering also enabled realization of functional thin film structures, such as superlattice which own novel physical properties compared to its original materials [16].

Recent development in strain engineering has opened a completely new era in condensed matter physics: utilization of strain engineering offers a novel method for

the manifest of novel physical phenomena. Since strain directly changes distance between each lattice, strain directly alters the electronic band structure of the material. As a result, spin-based physical phenomena is enormously sensitive to strain modification, and ultimately can manifest novel physical phenome. For example, spin-orbit interaction, a relativistic effect between nucleus and electron orbiting around nucleus, strongly affected by lattice-change-induced electronic band structure modification [17]. Recent studies reported the application of strain in surface state manipulation, creating and destroying topological state in Bi_2Se_3 [18]. In graphene, strain engineering manipulated graphene electronic state through creation of pseudo-magnetic field [19]. Thus, strain, which was 'to-be-removed' element in the thin film, has become a novel parameter in solid-state physics that can offer a new functionality and ultimately manipulate the physical phenomena.

1.3 Motivation of this research

Strain, with the recent development in its manipulation, may offer a new degree of freedom in spin-based condensed matter physics. As mentioned earlier, strain directly changes the distance between each atom in solid-state physics, modifying the electronic band structure and influencing the spin-orbit interaction enormously. As a result, a small change in strain can manifest huge changes in spin-based physical phenomena such as anomalous Hall effect, spin Hall effect and quantum spin Hall effect [20,21]. Conventional degrees of freedom has been remained in the conventional parameters such as temperature, pressure, electrical

and magnetic field. Strain, in that manner, allows another degree of freedom in spin-based physical phenomena.

Magnetic anisotropy, a directional dependence of magnetic properties in a material, is another candidate for physical phenomena in which strain can be utilized as a novel degree of freedom. Magneto-crystalline anisotropy, a fundamental magnetic anisotropy in ferromagnetic materials, is mainly based on the spin-orbit interaction, since the first order contribution is from the orbital motion of electrons coupled with crystal electric field. As a result, magneto-crystalline anisotropy is also very sensitive to changes in lattice constant. Since magneto-crystalline anisotropy determines magnetic properties of material such as coercivity and magnetic easy axis orientation, manipulation of magneto-crystalline anisotropy has significant important in both academic and industry.

GaMnAs, a Mn-doped GaAs, is highly advantageous material system in the research of magnetic anisotropy manipulation. First of all, since GaMnAs has comparably strong spin-orbit interaction, strain-based manipulation manifest stronger influence in magnetic anisotropy of the material. Second, GaMnAs has large Hall effect responses, ensuring high visibility of physical phenomena based on magnetic anisotropy. Finally, due to numerous previous studies, electrical methods for detection of magnetic anisotropy such as magnetoresistance are well established.

Researches on manipulation of magnetization in GaMnAs has been conducted by many groups, owing to the mentioned advantages of GaMnAs, but has been limited by the substrate. GaMnAs has in-plane magnetic easy axis under compressive strain and out-of-plane magnetic easy axis under tensile strain [22].

Different orientation of magnetization in GaMnAs thin film according to the strain has embarked numerous attempts to manipulate magnetization by changing the strain in the GaMnAs thin film. These attempts, started by growing GaMnAs film on the crystal with different lattice constant, include employment piezoelectric stage [23], bending the substrate and even relaxing strain by chemical etching [24]. However, strain manipulation in these studies were limited in magnitude and direction, due to the substrate. Strain manipulation by lattice-mismatch requires enormous number of sample growth in order to acquire significantly meaningful data. Method such as piezoelectric stage employment and substrate bending are limited by the substrate in its magnitude and direction of strain in order to prevent unrecoverable damage such as substrate fracture.

Nano-machining techniques can provide a novel method to manipulate strain in GaMnAs. Fabrication of freely suspended structure can manipulate the local strain of the thin film, with rest of the substrate untouched. Since Materials in smaller dimension exhibits higher failure strength [25], structures achieved by nano-fabrication can endure application of strain in much wider range. Furthermore, nano-structures, with incorporation of mechanical drive that can exert additional mechanical strain dynamically, may open the era of ‘physic-on-a-chip’ where measurement of physical phenomena under wide range of strain can be conducted in a single sample.

In magnetic systems with strong spin-orbit interactions such as GaMnAs, anisotropic magnetoresistance (AMR) is a direct manifestation of magneto-crystalline anisotropy. An understanding of the AHE and its intrinsic origins in

GaMnAs [26] has led to the development of a directly related spin Hall effect and other related relativistic effects, such as spin transfer torque. AHE measurements, along with the scaling relationship between the longitudinal conductivity and the Hall conductivity, demonstrate the intrinsic nature of GaMnAs [27] and have been shown to be sensitive to secondary phases [28].

Therefore, this dissertation attempts to manipulate the magnetic anisotropy of the GaMnAs epilayer by relaxing the strain of the GaMnAs structures fabricated by nano-machining technique and observe the changes in magnetic anisotropy through the measurement of anisotropy magnetoresistance (AMR) which includes anomalous Hall effect as well as planar Hall effect. At the same time, this dissertation attempts to determine the magnetic anisotropy the GaMnAs at zero strain which was not achieved due to the strain in the GaMnAs from pseudomorphic growth mechanism. Since relativistic spin-orbit interactions are highly sensitive to strain, a dynamic means of varying the local strain in GaMnAs may lead to a better understanding of magnetic anisotropy and serve as an avenue for adding new functionalities, stemming from mechanical degrees of freedom, to develop novel GaMnAs-based spintronic devices [29].

(Blank page)

2 Theoretical background.

In this chapter, theoretical background of this dissertation will be covered. Starting from ferromagnetism in GaMnAs, magnetoresistance including anomalous Hall effect and planar Hall effect in GaMnAs will be discussed. At the same time, Stoner-Wohlfarth model will be introduced and its modification for GaMnAs under compressive strain will be introduced.

2.1 Ferromagnetism in GaMnAs

After first proposal of ferromagnetic interaction model mediated by free carrier by Zener, it is widely accepted that the ferromagnetic ordering in GaMnAs is mediated by antiferromagnetic coupling between localized Mn ions and conduction holes in the valence band. GaMnAs consists of elements having atomic structure $[\text{Ar}]3d^{10}4s^2p^1$ for Ga, $[\text{Ar}]3d^54s^2$ for Mn, $[\text{Ar}]3d^{10}4s^2p^3$ for As. Since Mn^{2+} replaces Ga^{3+} in original GaAs lattice, two $4s$ electrons of Mn participates in crystal bonding in the same way as two $2s$ electrons in Ga. In electrically neutral state, Mn_{Ga} , Mn ion replacing Ga, has local moment with zero angular momentum and spin of $S=5/2$ which 5 electrons in the $3d$ shell that have the same spin orientation. As a result, Mn^{2+} ions have a total moment of $J = L + S = 0 + \frac{5}{2} = 5/2$. At the same time, Mn_{Ga} acts as an acceptor due to missing a $4p$ electron in valence band. Figure 2.1 illustrate lattice of GaMnAs where Mn ion replaces Ga.

Ferromagnetic ordering in GaMnAs can be explained by p - d exchange coupling between local moments and valence band holes of hosting GaAs. Figure 2.2 illustrate schematic picture of this p - d exchange. Spin-down of Mn d -shell level locates deep in the valence band while the spin-up d level, which is empty, is located above Fermi level. Hybridization of valence band $4p$ levels of GaAs and localized Mn d level elevates energy of spin-down valence band states relatively higher than spin-up valence band state [30]. As a result, p - d hybridization exerts spin dependent coupling between valence band holes and local Mn moments. However, carriers can be in a tightly bound state (with primarily d -character) or more spatially extended structure (with p -character). Since diluted magnetic moments exist in GaMnAs, the carrier mediated ferromagnetism requires acceptor level states which extend more than a few lattice constants by optimal hybridization strength between shallow and deep acceptor levels. Since Mn has a moderate acceptor level with binding energy of $E_a = 110$ meV in GaMnAs [9], energy difference between the parallel and antiparallel states of bound hole to Mn spin is relatively small, $\Delta\varepsilon = 8 \pm 3$ meV [9]. Despite of strong p - d hybridization, the hole from Mn ion does not occupy d -shell, and thus GaMnAs is classified as a charge-transfer insulator,

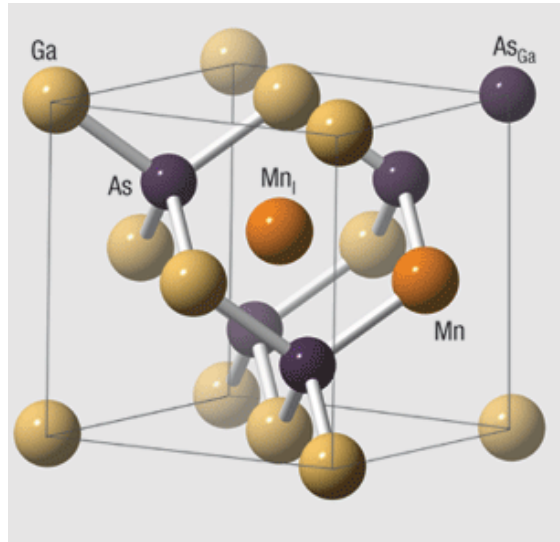


Figure 2.1 Lattice of GaMnAs with possible defects [31].

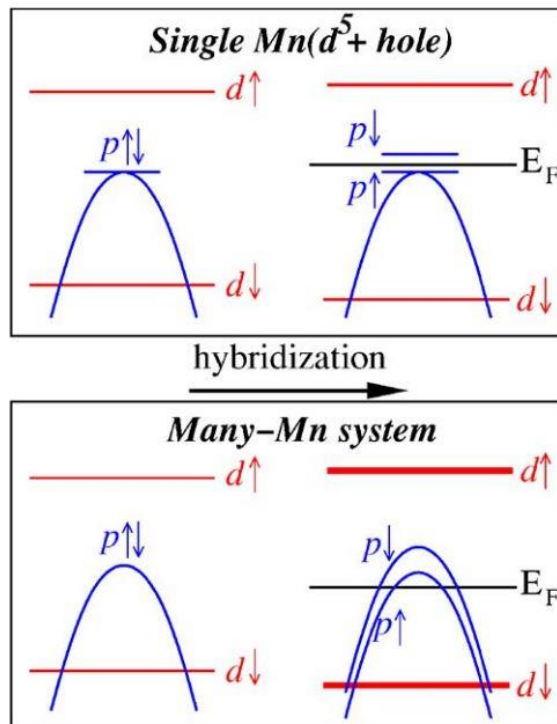


Figure 2.2 Splitting of the isolated Mn acceptor level (top) and splitting of the top of valence band in many-Mn system due to p - d hybridization (bottom) [9].

2.2 Magnetoresistance behavior in GaMnAs

Magnetoresistance, a physical phenomenon first discovered by William Thompson (or also known as Lord Kelvin) in 1956, is a response in electrical resistance in a material due to externally applied magnetic field [32]. Magnetoresistance may appear in various effects, including geometrical effects such as Shubnikov de Haas oscillation [33], positive magnetoresistance in metals [34] and negative magnetoresistance in ferromagnetic materials [35]. In multilayer system such as magnetic tunnel junction, magnetoresistance is an underlying basis for giant magnetoresistance (GMR), tunneling magnetoresistance (TMR) and extraordinary magnetoresistance (EMR) [36].

The physical origin of magnetoresistance is attributed to spin orbit coupling. Electron cloud around nucleus undergoes slight deformation as the direction of magnetization rotates. This deformation causes changes in the amount of scattering by conduction electrons while electrons travel through the lattice. According to heuristic explanation, magnetization rotates the closed orbit orientation with respect to the current direction. When external magnetic field and magnetization is transverse to the current, electronic orbits lies in the plane of current with small scattering cross-section and thus results in low resistance. On the contrary, when external magnetic field and magnetization is parallel to the current, since scattering cross-section is increased, resistance also increases [37]. Figure 2.3 illustrates this magnetoresistance response to different external magnetic field and figure 2.4 illustrates typical magnetoresistance response in metallic Co/Cu multilayer.

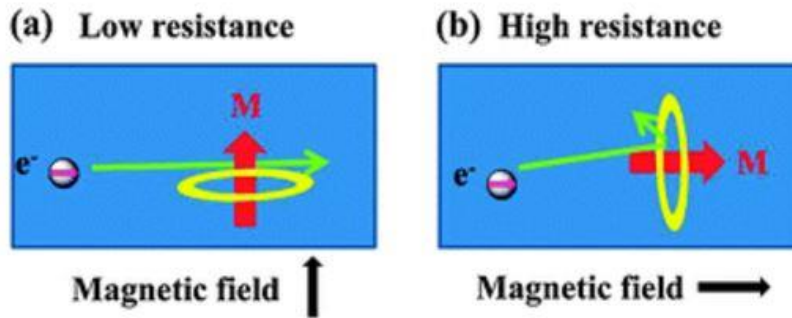


Figure 2.3 Schematic of magnetoresistance with (a) perpendicular magnetization and (b) parallel magnetization [37].

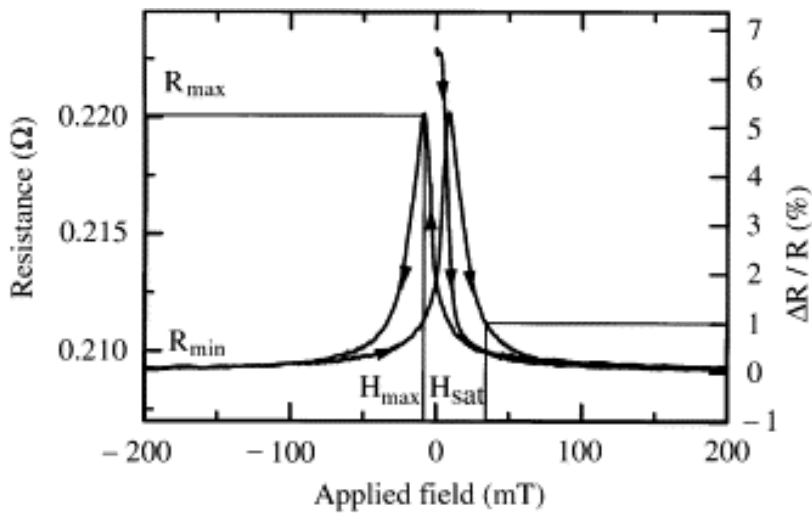


Figure 2.4 A typical plot of resistance vs. applied magnetic field in the Co/Cu multilayer [38].

GaMnAs, however, shows completely different magnetoresistance behavior compare to ordinary material described above. Anisotropic magnetoresistance (AMR) in GaMnAs appears in opposite shape to that of normal metal ferromagnetic materials. In other words, magnetoresistance is in low resistance state with parallel magnetization and high resistance state with transverse magnetization. Figure 2.5 shows typical AMR response from GaMnAs film. It is clearly shown that GaMnAs film with magnetization perpendicular to current direction is in the high resistance state, while GaMnAs film with magnetization parallel to current direction is in the low resistance state. According to Rushforth *et al.*, The noncrystalline AMR of GaMnAs is determined by combined effect of spin orbit coupled spin-texture in the host band and polarized scatters containing nonmagnetic and magnetic impurity potential [39]. From phenomenological decomposition of AMR in GaMnAs which extends standard phenomenology [40] to system with cubic and uniaxial anisotropy, which also correspond to Stoner-Wohlfarth model. Then longitudinal AMR can be expressed as following:

$$\frac{\Delta\rho_{xx}}{\rho_{av}} = C_1 \cos 2\phi + C_U \cos 2\psi + C_C \cos 4\psi + C_{I,C} \cos(4\psi - 2\phi) \quad (2.2.1)$$

where $\Delta\rho_{xx} = \rho_{xx} - \rho_{av}$, ρ_{av} is average of ρ_{xx} over 360° in the plane of the film, ϕ is angle between magnetization and the current, and ψ is the angle between magnetization and $[1\ 1\ 0]$ crystal structure [39]. Contributions in Eq. (2.2.1) are the noncrystalline term, the lowest order uniaxial crystalline term, the lowest order cubic crystalline term, and a crossed noncrystalline/crystalline term,

respectively. With consideration of two microscopic mechanisms for anisotropic carrier lifetimes, one related to polarization of randomly distributed magnetic scatters and the other related to polarization of the carrier band itself, former mechanism clearly dominate in the diluted moment system such as GaMnAs. Then, with proper simplification using spin-texture approximation, consideration of scattering off a δ -function potential $\propto (\alpha + \widehat{\mathbf{M}} \cdot \mathbf{s})$ and assumption of proportionality between conductivity and lifetime of carriers, following is obtained:

$$\frac{\sigma_{\widehat{\mathbf{M}}\parallel\mathbf{I}}}{\sigma_{\widehat{\mathbf{M}}\perp\mathbf{I}}} = \frac{(\alpha^2 + \frac{1}{4})(\alpha^2 + \frac{1}{12})}{(\alpha^2 - \frac{1}{4})^2} \quad (2.2.2)$$

where σ is conductivity and α represents the ratio of nonmagnetic and magnetic parts of the impurity potential [39]. For metallic ferromagnet, where $\alpha \ll 1$, $\sigma_{\widehat{\mathbf{M}}\parallel\mathbf{I}} < \sigma_{\widehat{\mathbf{M}}\perp\mathbf{I}}$ is expected and usually observed. However, when α is no longer negligibly small as in GaMnAs (i.e. $\alpha = \frac{1}{\sqrt{20}}$), the sign of noncrystalline AMR reverses at a relatively weak nonmagnetic potential and its magnitude is maximized when two terms are comparable (i.e. $\alpha = \frac{1}{2}$) [39].

In thin-film-based magnetic material system such as GaMnAs, anisotropic magnetoresistance can be categorized into two physical effect according to orientation of applied magnetic field. When applied magnetic field is perpendicular to the surface of the thin film (or out-of-plane), which is identical geometry to the Hall effect, anomalous Hall effect appears with ordinary Hall effect. On the other hand, when applied magnetic field is parallel to the surface of the thin film (or in-

plane), planar Hall effect occurs. Both the anomalous Hall effect and the planar Hall effect are based on anisotropic magnetoresistance and will be discussed in the following sections.

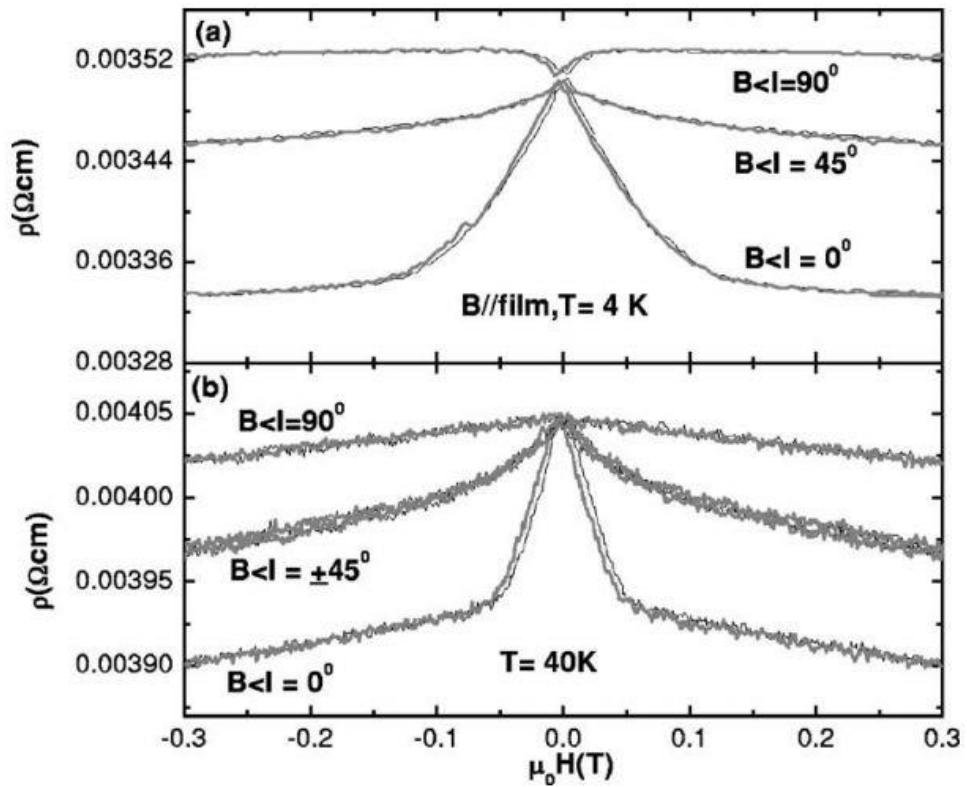


Figure 2.5 The in-plane anisotropic magnetoresistance at (a) 4.2 K and (b) 40 K for the as-grown $\text{Ga}_{1-x}\text{Mn}_x\text{As}$ thin film with $x = 0.034$ when current lies in the $[110]$ direction [41].

2.2.1 Anomalous Hall Effect in GaMnAs

The ordinary Hall effect which was proposed by Edwin H. Hall in 1879 state that a small transverse electric field (E_H) is proportional to the product of primary current density (I_D) an the component of magnetic field flux (B_Z) [42]. Thus ordinary Hall effect can be express as:

$$E_H = RI_D B_Z \quad (2.2.1.1)$$

where R is the Hall coefficient. However, in case of ferromagnet, a response to spontaneous magnetization which is no longer proportional the applied field, namely anomalous Hall effect (AHE), must considered. As a result, the Hall resistivity (ρ_{xy}) has an empirical relationship expressed as sum of resistivity correspond to ordinary Hall effect (ρ_{xy}^{OHE}) and resistivity correspond to anomalous Hall effect (ρ_{xy}^{AHE}) as shown below:

$$\rho_{xy} = \rho_{xy}^{OHE} + \rho_{xy}^{AHE} = R_0 B_Z + R_S M \quad (2.2.1.2)$$

where B_Z is applied magnetic field, M is magnetization, R_0 and R_S are ordinary and anomalous Hall coefficient, respectively. This empirical relation between the magnetization and Hall resistivity was independently proposed by Smith and Pugh, four decades after the discovery of AHE [43-45]. Figure 2.6 illustrates schematically how addition of anomalous Hall component effect the Hall response of the material.

Origin of anomalous Hall effect can be divided into two composition: intrinsic and extrinsic Hall effect. Intrinsic anomalous Hall effect was investigated by Kaplus and Luttinger from intrinsic spin-orbit interaction for itinerant spin polarized electrons, suggesting acquisition of group velocity for electrons with external electric field [46]. Due to its perpendicularity to electric field, this anomalous velocity contribute to the Hall effects and in case of ferromagnetic conductor, the sum of the anomalous velocity can be nonzero and thus contribute to transverse Hall conductivity. This type of contribution in anomalous Hall effect only depend on the band and thus expressed completely in terms of the Bloch function of the host crystal, and transverse conductivity is independent of the impurity concentration [47-49], yielding AHE contribution to $\rho_{xy} \approx \sigma_{xy}/\sigma_{xx}^2$ and therefore proportional to ρ^2 . However, intrinsic component proposed by Kaplus and Luttinger centered on the complete absence of scattering from disorder, while materials such as GaMnAs inevitably affected by disorder incorporated during Mn doping. Extrinsic contribution of anomalous Hall effect, which considers effects of these disorder in the system, can be divided into two scattering mechanism: ‘skew-scattering’ and ‘side-jump’. Skew-scattering, proposed by Smit in 1958, attributes extrinsic anomalous Hall effect to asymmetric spin dependent skew scattering of free carriers by impurity by the mean of spin-orbit interaction [50,51]. Skew scattering is an asymmetric scattering of an electron with respect to the plane containing its incident velocity and the ion’s magnetic moment and thus the anomalous Hall resistivity is linearly proportional to the longitudinal resistivity ($R_s \sim \rho_{xx}$). On the other hand, side-jump, suggested by Berger in 1970, is the result of quantum mechanical

perspective and results in a constant lateral displacement from its original path through scattering center, owing quadratic dependency to longitudinal resistivity [52,53]. In other words, side-jump mechanism is a consequence of anomalous velocity mechanism in Kaplus and Luttinger theory acting while a quasiparticle was under the influence of the electric field due to an impurity [54]. Thus, contribution from side-jump mechanism is proportional to square of longitudinal resistivity ($R_s \sim \rho_{xx}^2$), which is identical to that from intrinsic mechanism by Kaplus and Luttinger. Figure 2.7 illustrates origins of these three main mechanism in anomalous Hall effect.

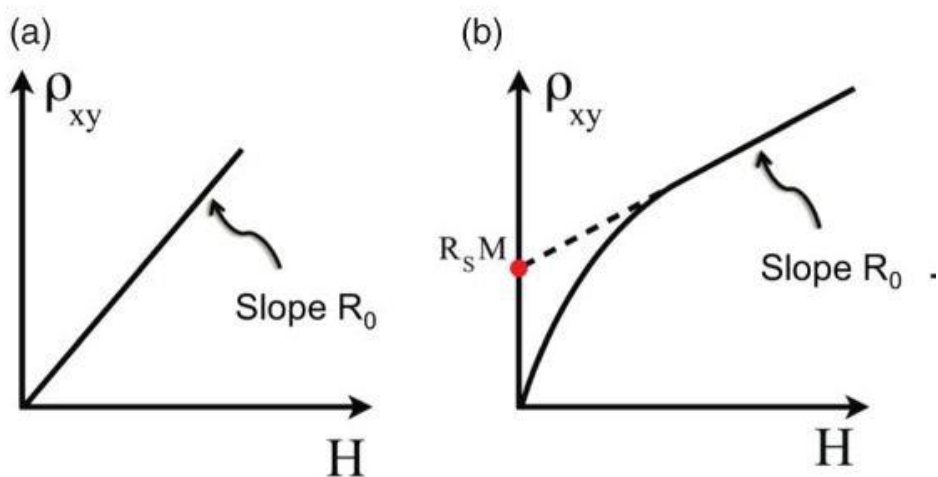


Figure 2.6 Schematic illustration of (a) the Hall effect and (b) the anomalous Hall effect [55].

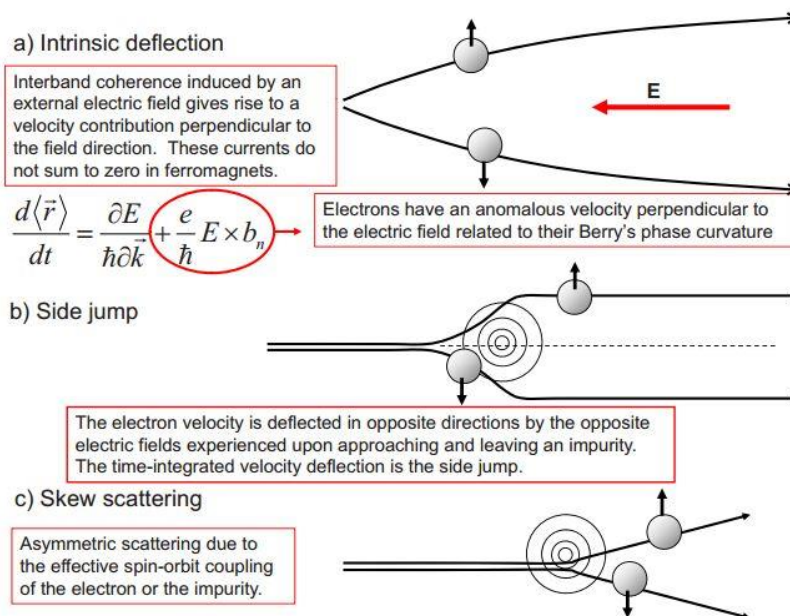


Figure 2.7 Illustration of the three main mechanism of anomalous Hall effect [54].

2.2.2 Stoner-Wohlfarth model

Stoner-Wohlfarth model (SW model), developed by Edmund Clifton Stoner and Erich Peter Wohlfarth in 1948, provides a simple, but powerful explanation for magnetization of a single-domain ferromagnet and its magnetic hysteresis [56]. As shown in the subset of Fig. 2.8, in Stoner-Wohlfarth model, a structure (in this case Hall bar) is considered as a single-domain magnet. When a magnetic field is applied to a ferromagnet (FM), a magnetization change occurs and when applied magnetic field is swept, hysteresis loop occurs in magnetization vs. applied magnetic field (\mathbf{M} vs. \mathbf{H}) plot, as shown in Figure 2.8. The main characteristics of \mathbf{M} vs. \mathbf{H} are saturation magnetization M_S , the remnant magnetization M_r , and coercive field H_C . The saturation magnetization is the magnetization when all the magnetic moments are aligned along certain common direction, resulting the largest value of the magnetization. The remnant magnetization is the magnetization when applied magnetic field is zero and thus signifies the leftover magnetization after removal of applied magnetic field. The coercive field is the strength of applied magnetic field required to reverse the magnetization of FM. The ratio M_r/M_S , usually called squareness approaches value of 1 when applied magnetic field is aligned in the certain direction defined as the easy axis (EA) and in this case the hysteresis loop becomes closest to a square shape. When the angle ϕ , the angle between applied magnetic field and easy axis, is increased the opening of the hysteresis loop is reduced. The opening of hysteresis loop in \mathbf{M} vs. \mathbf{H} plot is largest when the magnetic

field is most parallel to the EA and smallest when the magnetic field is most parallel to the hard axis, which is usually perpendicular to the EA in simple system.

According to SW model, at $T = 0$ K a grain carrying a single moment \mathbf{M} , is an ellipsoid-shaped object since a material with uniform magnetization ought to have an ellipsoid form [57]. This grain possesses a uniaxial anisotropy (corresponds to an axis along which the magnetization prefers to lie in order to minimize the energy) and is subjected to an externally applied static magnetic field \mathbf{H} . Evolution of magnetization \mathbf{M} is strictly limited in two-dimensional space and angle between magnetization and magnetic easy axis θ and the angle between applied magnetic field and easy axis ϕ becomes the main variables in SW model. Thus, the magnetic moment \mathbf{M} is subject to two competing aligning forces: one due to the uniaxial anisotropy and the other due to external magnetic field \mathbf{H} . Therefore, the total energy is the sum of anisotropic energy E_A and the Zeeman energy $E_Z = -\mathbf{M} \cdot \mathbf{H}$, and can be expressed as following:

$$E = E_A + E_Z = K\sin^2\theta - HM\cos(\theta - \phi) \quad (2.2.2.1)$$

where K is anisotropic constant.

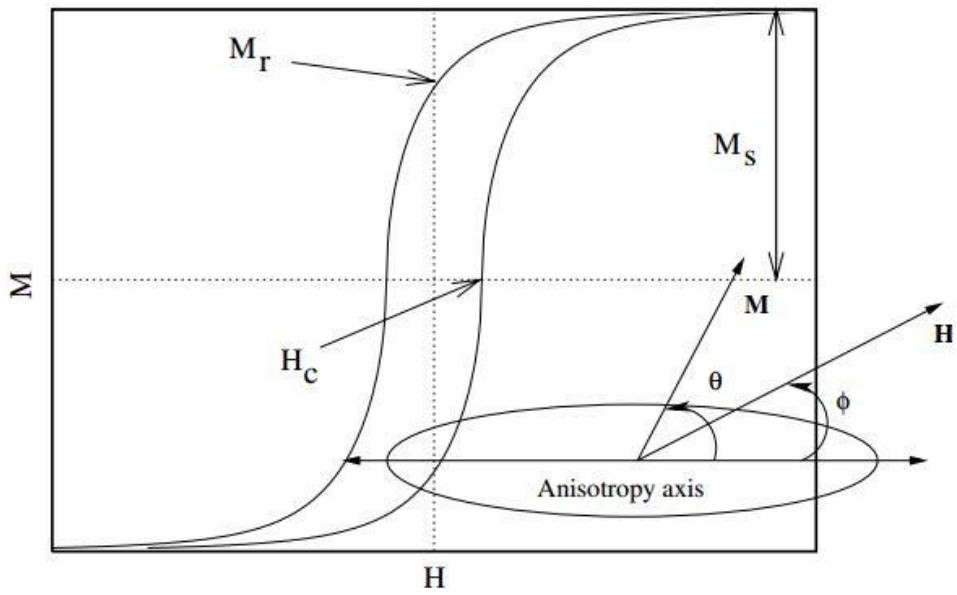


Figure 2.8 Single domain hysteresis loop obtained for an arbitrary angle between the magnetic field and the anisotropy axis ϕ [57].

In case of GaMnAs, a few modification must be made in ordinary SW model, considering both uniaxial and biaxial anisotropy in GaMnAs film. Furthermore, in the case of microstructure based of GaMnAs a shape anisotropy must be considered as well. These modifications and underlying physics will be discussed in following section.

2.2.3 Shape anisotropy and strain-based anisotropy

Although magnetic anisotropy is an intrinsic property of material, it can be also induced by a shape of the structure or by the strain induced to the structure. In a polycrystalline ferromagnetic material, if width and length of the material are different from each other, magnetization in that material tends to align toward long axis of the material. This phenomenon, so-called shape anisotropy, can be understood by the demagnetization field. Figure 2.9 illustrates the shape anisotropy in a prolate pheroid of Co and Figure 2.10 illustrate the demagnetization factors for different shapes. Demagnetization field generated by the magnetization of ferromagnetic material has direction opposite to the magnetization direction and amplitude proportional to the amplitude of magnetization. The demagnetization field can be expressed as following:

$$\mathbf{H}_d = N_d \mathbf{M} \quad (2.2.3.1)$$

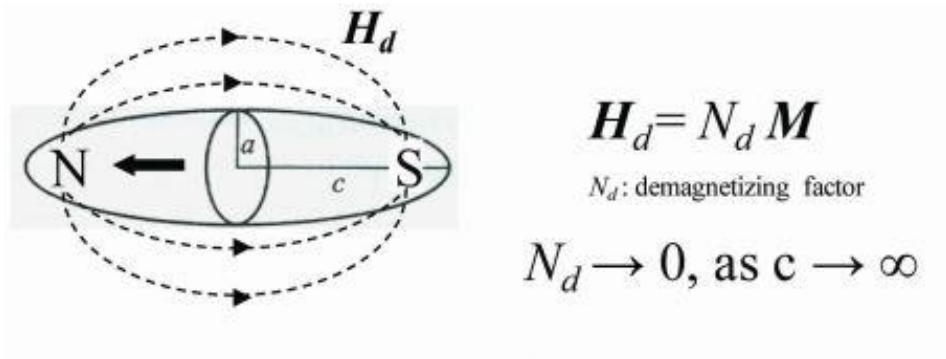


Figure 2.9 Shape anisotropy in a prolate spheroid of Co [58].

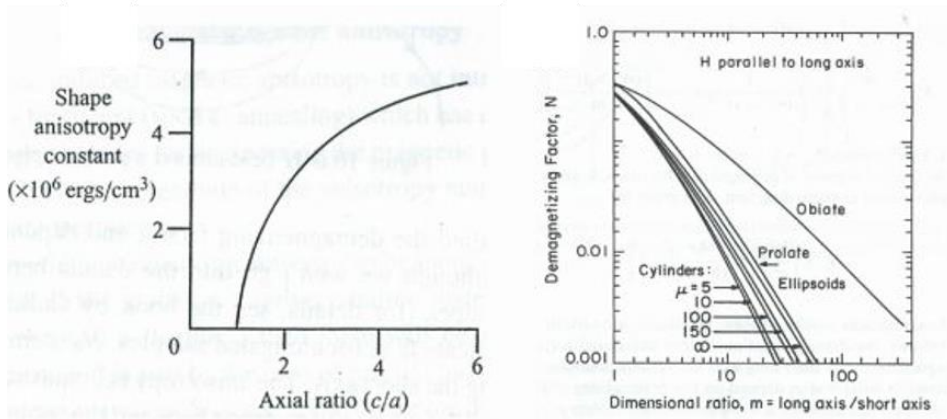


Figure 2.10 (Left) Shape anisotropy constant in prolate spheroid [58]. (right) Demagnetization factor for different shapes [59].

where H_d is the demagnetization field, N_d is the demagnetization factor, and M is the magnetization [58]. The shape of the ferromagnetic material determines the demagnetization factor. As shown in the Figure 2.10, shape anisotropy constant approaches 1 as ratio of width and length approaches unity and demagnetization factor converses to zero as the length of the material increases.

Strain also plays important role in magnetic anisotropy in GaMnAs, due to the spin orbit interaction in the hole valence bands. Figure 2.11 shows how strain in the material effects the band structure of epilayer. Since growth of GaMnAs is pseudomorphic growth process, grown film inevitably owns a strain. This strain generally decomposed into hydrostatic strain and shear strain. For cubic crystal structure, hydrostatic only shift energy level without symmetry breaking. However, shear strain causes band degeneracy lifting and band warping and thus regarded more important in device engineering [60].

When coupled with electron spin, the eigenstate at $k=0$ split into fourfold multiplet ($J = 3/2, m_J = \pm 3/2, \pm 1/2$) and twofold multiplet ($J = 1/2, m_J = \pm 1/2$). In conventional semiconductor, which is under no effective strain, hole in the $\left| \frac{3}{2}, \pm \frac{1}{2} \right\rangle$ state has effective mass smaller than the hole in the $\left| \frac{3}{2}, \pm \frac{3}{2} \right\rangle$ state. Former is called light hole-bands and latter is called heavy hole-bands. Under strain, different hole-bands moves up and determines bandgap: light or heavy hole-bands moves up and for tensile strain and compressive strain, respectively. The energy shifts can be expressed in terms of lattice strain as following:

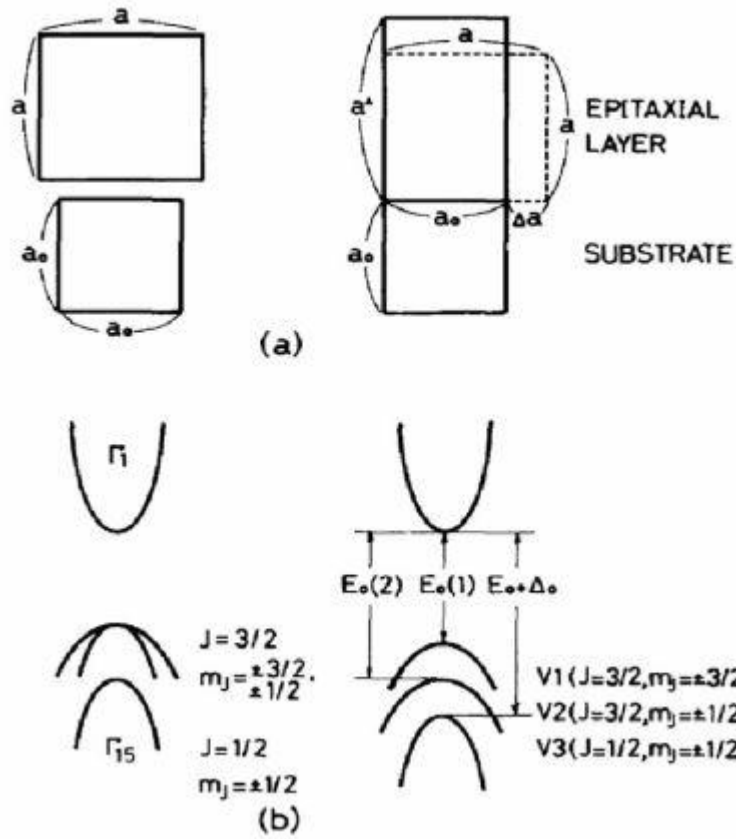


Figure 2.11 Schematics representing (a) unstrained and deformed lattice and (b) corresponding band structure changes [61].

$$\Delta E_L \left(\frac{3}{2}, \pm \frac{1}{2} \right) = \frac{e_0}{c_{11}} \left[-2a_1(C_{11} - C_{12}) + \frac{a_2}{2}(C_{11} + 2C_{12}) \right] \quad (2.2.3.2)$$

$$\Delta E_H \left(\frac{3}{2}, \pm \frac{3}{2} \right) = \frac{e_0}{c_{11}} \left[-2a_1(C_{11} - C_{12}) - \frac{a_2}{2}(C_{11} + 2C_{12}) \right] \quad (2.2.3.3)$$

where e_0 is the in-plane strain induced by lattice mismatch in substrate-film given by $e_0 = (a_{\text{substrate}} - a_{\text{film}})/a_{\text{film}}$, C_{ij} are the elastic constant of unstrained film, a_1 and a_2 are hydrostatic and shear deformation potential, respectively [62]. Then, magnetic anisotropy energy due to strain can be obtained by perturbative correction to the effective Zeeman coupling shown below:

$$\mathbf{h} = J_{pd} N_{Mn} \mathbf{M} \quad (2.2.3.4)$$

where J_{pd} is exchange coupling between valen band hole and localized moment, N_{Mn} is the number of magnetic impurities per volume. Then anisotropic energy due to strain can be obtained using (2.2.3.2.) and (2.2.3.3) and given as following:

$$\frac{E_{\text{strain}}(M)}{V} = \frac{p}{4} [3\Delta E_H + \Delta E_L] + \frac{3p \cos^2 \theta}{4} [\Delta E_H - \Delta E_L] \quad (2.2.3.5)$$

where p is hole density. Figure 2.12 shows strain dependence of magnetic anisotropy energy at hole density of $p=0.35 \text{ nm}^{-3}$. For compressive strain, where $e_0 < 0$, the system has an easy axis in-plane. On the contrary, for tensile strain, where $e_0 > 0$, the anisotropy is easy axis along growth direction which is out-of-plane. Additionally, the anisotropy changes its sign at large tensile strain [63]. It is also notable that strain in very small quantity as 1% are sufficient to change the magnetic anisotropy completely.

Orientation of magnetic easy axis in GaMnAs, which is strongly depend on the strain orientation within the film, has been reported experimentally. Figure 2.13 illustrates Hall resistance in GaMnAs with different film grown underneath GaMnAs. When GaMnAs is grown on GaAs, which has larger lattice constant compare to GaMnAs, GaMnAs experience compressive strain and magnetic easy axis lies within the plane. On the other hand, when GaMnAs is grown on InGaAs, which has smaller lattice constant compare to GaMnAs, GaMnAs experience tensile strain and magnetic easy axis is perpendicular to the plane. These experimental results corresponds to the theoretical estimation.

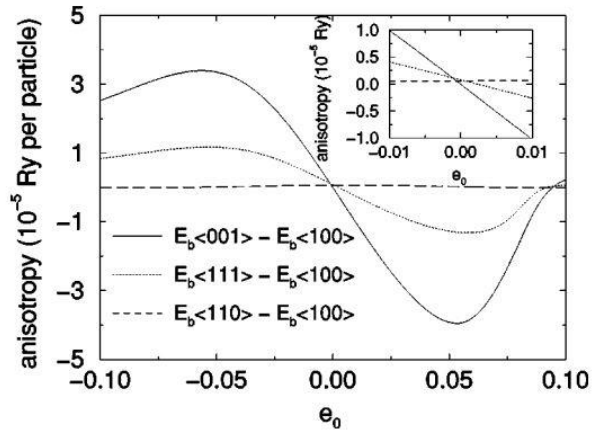


Figure 2.12 Energy differences among different magnetization orientations versus in-plane strain e_0 [63].

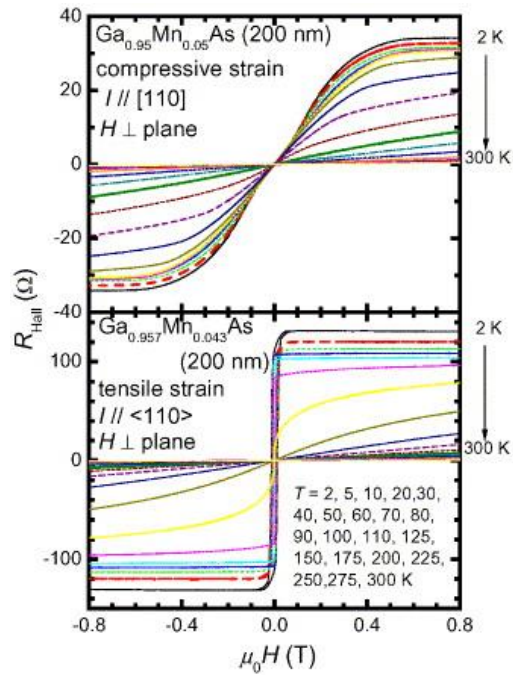


Figure 2.13 Hall resistance at various temperature between 2 and 300 K for (top) $\text{Ga}_{0.95}\text{Mn}_{0.05}\text{As}/\text{GaAs}$ (compressive strain) and (bottom) $\text{Ga}_{0.957}\text{Mn}_{0.043}\text{As}/(\text{In},\text{Ga})\text{As}$ (tensile strain) [22].

2.2.4 Modification of Stoner-Wohlfarth for GaMnAs under compressive strain

GaMnAs film under compressive strain, as mentioned above, has magnetic easy axis within the plane. In addition, there are two magnetic anisotropy in GaMnAs under compressive strain: biaxial anisotropy which is along GaAs [1 0 0] and [0 1 0] and uniaxial anisotropy which is along GaAs [1 1 0] [64]. These two magnetic anisotropy are competing component in magnetic anisotropy of GaMnAs [65] and this competition between two magnetic anisotropy strongly depends on Curie temperature (T_C). The orientation of the magnetic moments changes through a second-order transition, or so-called continuous transition, from a biaxial dominant mode below $T_C/2$ to an axial dominant mode above $T_C/2$. This transition is a result of the interplay between the natural cubic anisotropy of the GaMnAs zinc-blende structure and a uniaxial anisotropy which attribute to the effects of surface reconstruction [64]. Thus, modification must be made to Stoner Wohlfarth model in (2.2.2.1) which only considered uniaxial anisotropy, adding additional term for biaxial anisotropy.

Since GaMnAs own two magnetic anisotropy, uniaxial anisotropy along [1 1 0] and biaxial cubic anisotropy along [1 0 0] and [0 1 0] direction, both anisotropy contributes to the magnetic anisotropy of GaMnAs. Then, corresponding free energy density of such a single domain ferromagnet can be written as following:

$$E = K_U \sin^2 \theta_M + \frac{K_C}{4} \cos^2 2\theta_M - MH \cos(\theta_M - \theta) \quad (2.3.3)$$

where K_U is in-plane uniaxial magnetic anisotropy constant, K_C is in-plane biaxial cubic magnetic anisotropy constant, θ_M and θ are angle of magnetization and applied field relative to current direction, respectively. Then equilibrium state, or local minima is defined by conditions, $\frac{\partial E}{\partial \theta_M} = 0$ and $\frac{\partial^2 E}{\partial \theta_M^2} > 0$. This give us equation for the equilibrium state which is expressed as:

$$K_U \sin 2\theta_M + K_C \sin 4\theta_M + MH \sin(\theta_M - \theta) = 0 \quad (2.3.3)$$

Then four local energy minima can be estimated to be:

$$\theta_M = \pm \left(\frac{\pi}{4} - \delta \right), \pm \left(\frac{3\pi}{4} + \delta \right) \quad (2.3.4)$$

where $\delta = \sin^{-1} K_U/K_C$. Figure 2.14 shows energy landscape estimated from Stoner-Wohlfarth model.

Then electric field within the single domain ferromagnetic Hall bar with in-plane magnetization can be written as below:

$$E_x = j\rho_{\perp} + j(\rho_{\parallel} - \rho_{\perp}) \cos^2 \theta_M \quad (2.3.1)$$

$$E_y = j(\rho_{\parallel} - \rho_{\perp}) \sin \theta_M \cos \theta_M \quad (2.3.2)$$

where j is current density (assumed to be uniformly distributed along Hall bar, E_x and E_y are longitudinal and transverse electric field, respectively, θ_M is angle between magnetization and current density, ρ_{\parallel} and ρ_{\perp} are the resistivities for current oriented parallel and perpendicular to the magnetization [66].

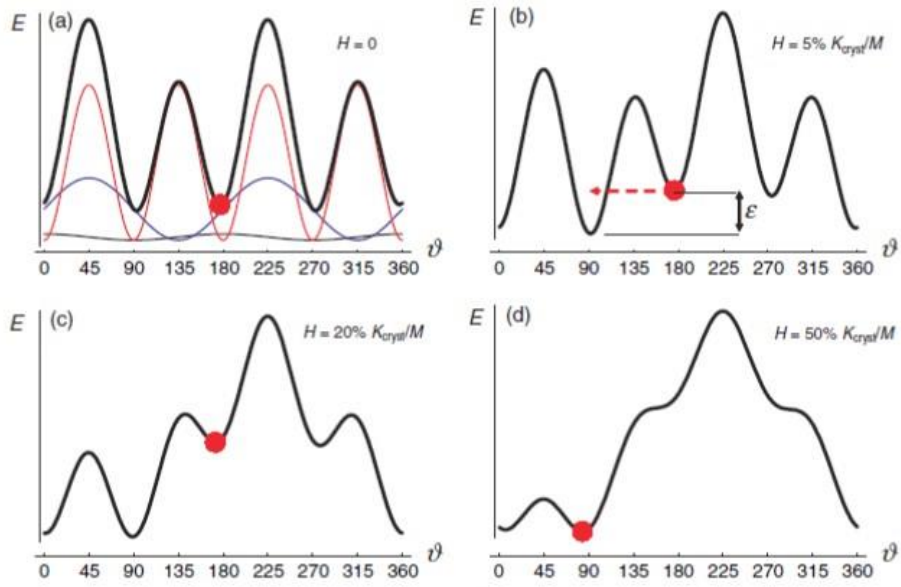


Figure 2.14 (a) Energy landscape at zero field estimated from biaxial (red) and uniaxial (blue). (b)-(d) evolution of energy surface with increasing field [67].

(Blank page)

3 Sample Preparation

In this chapter, a full process from growth of GaMnAs/GaAs/AlGaAs/GaAs by molecular beam epitaxy (MBE) to the fabrication of freely-suspended GaMnAs nanostructure will be described. By optimizing concentration of Mn and Al in GaMnAs and AlGaAs as well as growth temperature of GaMnAs, GaMnAs/GaAs/AlGaAs/GaAs structure is realized. With incorporation of metallic electrical leads, application of delicately-controlled e-beam lithography and chemical etching enables the fabrication of freely-suspended GaMnAs structure with significantly reduced strain.

3.1 MBE-growth of LT-GaMnAs/LT-GaAs/AlGaAs/GaAs structure

3.1.1 Introduction of MBE growth

Molecular beam epitaxy (MBE) is a growth technique for thin, epitaxial films in an ultra-high vacuum(UHV) environment. MBE growth technique had been widely adapted to growth of thin semiconductor film since 1970s [68]. MBE techniques has been a sophisticated technique for epitaxial film growth with high crystallinity which is attributed to its high-purity source material and UHV environment. Figure 3.1 illustrated a scheme of a typical MBE system. MBE system

consist of six parts; source oven, beam shutters, substrate holder/heater, *in-situ* growth characterization system, beam flux monitoring system and cryopanel. In ordinary MBE system, source oven usually consists of several effusion cells and each cell contains pure single-element source material. In case of LT-GaMnAs/LT-GaAs/AlGaAs/GaAs structure, minimum of 4 effusion cells (Ga, As, Mn, Al) are required. Main function of source oven is to generate a molecular beam from source material by the mean of thermal evaporation. Separation of each source ensures precise control of composition during the growth process. However, current MBE system has expanded its application and some MBE systems are equipped unconventional source oven such as one with metal-organic source (MO-source) or plasma source. Beam shutters allow/prevent individual molecular beam from each source oven to/from arriving substrate. Use of beam shutters enables selection of molecular beams impinging on the substrate. Substrate holder/heater hold the substrate for the growth and enables temperature control of the substrate. *In-situ* growth characterization system monitors the quality or the growth mode simultaneously. Typical apparatus of *in-situ* growth characterization system is reflection of high energy electron diffraction (RHEED) which accelerated electron (typically 5 ~ 100 kV) impinges upon the substrate with very small incident angle (angle between substrate plane and the electron trajectory) and corresponding reflected electron reaches phosphorescent screen, forming RHEED pattern. Furthermore, as shown in figure 3.2, RHEED oscillation provides a mean of characterizing growth rate, enabling layer-by-layer control of growth [69]. Beam flux monitoring system, typically a Bayard-Alpert ionization gauge (also known as

ion gauge), measures partial pressure of each molecular beam and allows precise and delicate control of each molecular beam. Cryopanel, isolated portion of vacuum chamber supplied by liquid nitrogen (LN₂), act as an additional pumping system which reduce the kinetic energy of gas molecule in the vacuum chamber. Use of cryopanel in MBE system critically minimizes unintentional doping during growth process.

Film quality enhancement in MBE growth is attributed to UHV environment, cryopanel and *in-situ* growth characterization system. UHV environment of MBE system, typically base pressure of $10^{-9} \sim 10^{-10}$ Torr, ensures significantly reduced partial pressure of H₂O, CO₂, and CO. Use of cryopanel, by significantly reducing kinetic energy of gas molecule significantly, prevents molecules other than ones from source oven arriving the substrate. Additionally, *in-situ* growth characterization system such as RHEED, enables monitoring growth mode and crystallinity of grown film simultaneously during the growth process.

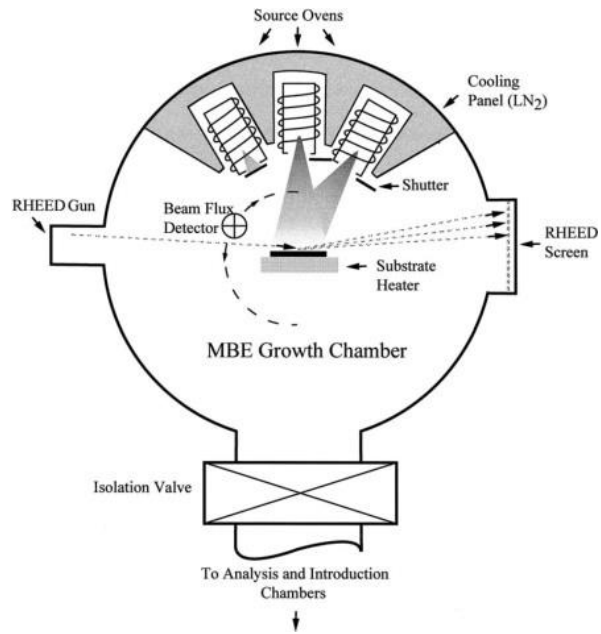


Figure 3.1 Schematics of typical MBE system [68].

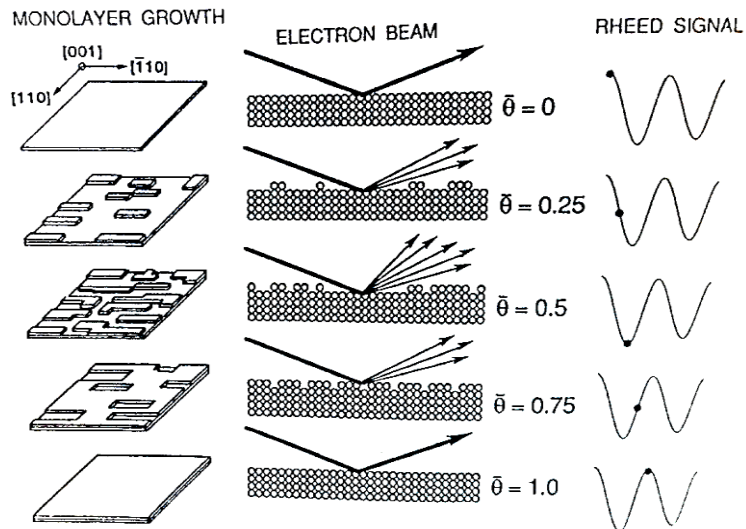


Figure 3.2 Mechanism of RHEED specular spot oscillation during growth [69]

3.1.2 Growth of LT-GaMnAs/LT-GaAs/AlGaAs/GaAs

Fabrication of freely-suspended structure, incorporation of suitable sacrificial layer between substrate and GaMnAs layer is necessary. Sacrificial layer requires two conditions; etching selectivity and lattice-compatibility. Material used in sacrificial layer should be able to be etched by an etchant in which GaMnAs layer does not react to. At the same time, sacrificial layer must have a lattice constant close to substrate and GaMnAs so that insertion of sacrificial layer does not cause significant lattice-mismatch. AlGaAs with lattice constant $\sim 5.6534 \text{ \AA}$ (lattice constant of GaAs $\sim 5.6533 \text{ \AA}$) has been selected as a sacrificial layer [70].

Growth of LT-GaMnAs/ LT-GaAs/AlGaAs/GaAs has been conducted in Riber 32 system equipped with four effusion cells with high purity element sources (Ga(99.9999 %), Mn(99.999%), As(99.9999%), and Al(99.9999%) in a standard 35 cc PBN crucible). Growth chamber maintained at UHV environment with base pressure $\sim 1 \times 10^{-9}$ Torr at stand-by and $\sim 1 \times 10^{-8}$ Torr during growth. For *in-situ* growth characterization, a 12 keV RHEED system was utilized. Flux of each element molecular beam was measured before growth and found to be 1.7×10^{-7} Torr for gallium, 1.5×10^{-7} Torr for aluminum, 5.0×10^{-8} Torr for manganese and 5.2×10^{-6} Torr for arsenic. Flux of arsenic was decided so that As₄/Ga flux ratio becomes 30 [71]. Flux of manganese and flux of aluminum were targeted for 6% of Mn concentration in GaMnAs and 75% of Al concentration in AlGaAs, respectively. An epi-ready GaAs (001) substrate was indium-mounted on the molybdenum substrate holder. All substrate was pre-baked in UHV pre-bake chamber at 150 °C for an hour.

Figure 3.3 illustrates schematics and RHEED pattern for each grown layer [72]. First of all, temperature of substrate was raised for residual oxide desorption. Residual oxide desorption was monitored using RHEED system in which 2×1 surface reconstruction pattern appears after desorption process. A homoepitaxy-growth of 300 nm GaAs was conducted for buffer layer at the temperature of 600 °C. Throughout RHEED specular spot oscillation, growth rate of GaAs was measured to be 300 nm/hr. Then 3 μm AlGaAs sacrificial layer was grown at the same temperature. After growth of sacrificial layer, temperature of substrate is lowered to 200 °C for low-temperature (LT) GaMnAs growth. As shown in figure 3.4, GaMnAs growth requires low temperature growth, otherwise segregation of unwanted secondary phase such as MnAs occurs due to low solubility of Mn in GaAs [73,74]. Prior to growth of GaMnAs, 10 nm low-temperature GaAs (LT-GaAs) which serves as buffer for GaMnAs has been grown at 200 °C. Additional insertion of GaAs (~50 nm) buffer layer between AlGaAs layer and LT-GaAs layer enhances quality of film grown in low-temperature. After growth of LT-GaAs, GaMnAs growth was started by opening shutter for Mn effusion cell and 200 nm GaMnAs was grown. Throughout growth process, growth mode and quality of each layer was monitored by *in-situ* RHEED images. As shown in Figure 3.3, surface reconstruction along $[1\ 1\ 0]$ and $[\bar{1}\ 1\ 0]$ crystal directions are observed. As each layer is grown, RHEED images changes and reflects crystal structure of each layer. As mentioned earlier, streaky patterns in each image implies that surface atoms are arranged into surface structure in 2-D growth mode by mean of surface diffusion. Furthermore,

typical '1x2' surface reconstruction appeared during GaMnAs growth indicates layer-by-layer single phase epitaxial growth of GaMnAs.

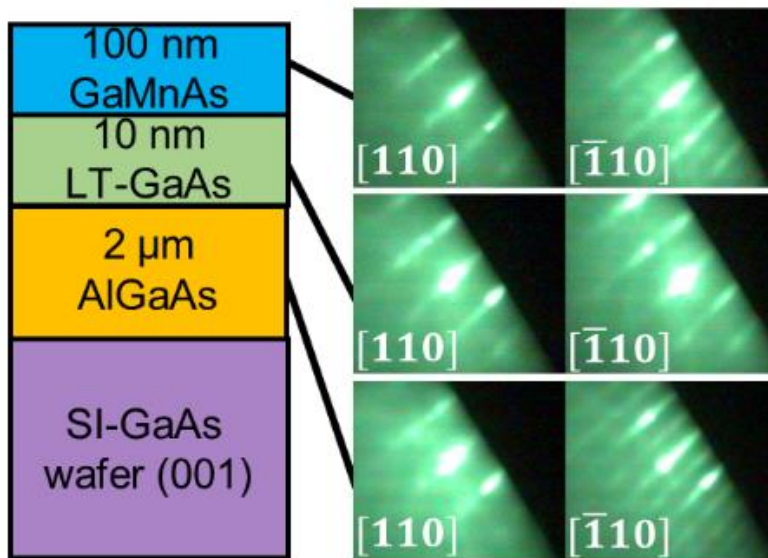


Figure 3.3 Schematics of structures and corresponding RHEED images [72].

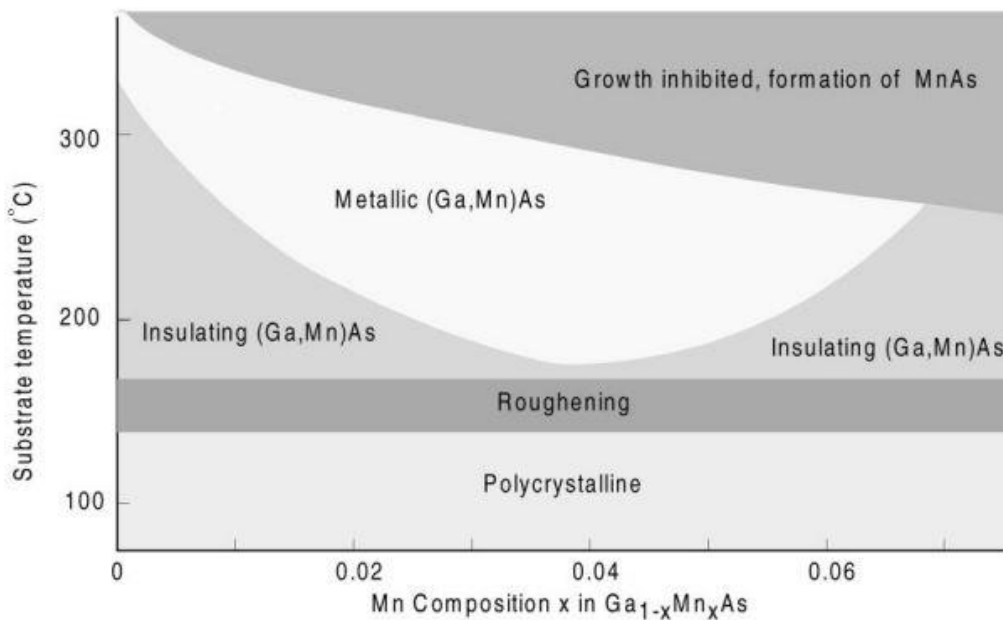


Figure 3.4 GaMnAs phase diagram [73].

3.2 Characterization of LT-GaMnAs/LT-GaAs/AlGaAs/GaAs

3.2.1 Post-Annealing

After growth, the sample were annealed in a tube furnace with a flow of N₂ gas. Post-growth annealing, by supplying sufficient energy for diffusion within the sample, significantly reduces impurity or defect site due to interstitial Mn (Mn_i), Mn-Mn complexes, As antisites, vacancy at As site and Mn-As complexes. For determination of optimal post-annealing temperature, samples were annealed at 250 °C, 300 °C and 350 °C in the tube furnace for an hour with N₂ flow of 300 cc/min. Then a standard Hall bar geometry (300 μm x 1900 μm) was fabricated on each sample by standard photo-lithography. Then samples are mounted into 10K closed-cycle cryostat for resistance vs. temperature measurements. All measurements were conducted by Keithley 2400 with direct current of 1 μA and longitudinal resistances were measured.

Figure 3.5 illustrates resistance vs. temperature (R vs. T) of samples annealed at different temperature. As shown in figure 3.5, post-annealing at 250 °C and 300 °C (thermocouple at tube furnace) reduced resistance of the sample significantly. However, post-annealing at 350 °C resulted in resistance increase, suggesting optimal post-annealing temperature for the sample to be 250 ~ 300 °C. This reduction of longitudinal resistance below certain temperature, in our case ~300 °C, can be attributed to reduction of donor impurity such as Mn_i by out-diffusion to

the surface and/or passivated [75]. Increase of longitudinal resistance above this temperature can most likely be attributed to the decrease in Mn concentration. Reduction and increase in longitudinal resistance accord with previous study [27]. From above result, optimal post-annealing temperature was determined to be 300 °C (thermocouple in the tube furnace).

3.2.2 Determination of Mn and Al concentration

Prior to fabrication, concentration of Mn and Al in GaMnAs and AlGaAs were determined by Bruker D8 Advance high resolution X-ray diffraction (HR-XRD) at room temperature using Cu- $K\alpha$ radiation. As depicted in Figure 3.5, θ - 2θ scan of sample clearly shows three diffraction peaks which is attributed to reflection from GaMnAs (004), AlGaAs (004) and GaAs (004) substrate. From each peak position, lattice constant for each layer (a_{XRD}) can be estimated using following;

$$a_{\text{XRD}} = \frac{\lambda}{2 \sin \theta} \sqrt{h^2 + k^2 + l^2} \quad (3.2.1.1)$$

where λ is wavelength of X-ray ($\lambda_{\text{Cu-K}\alpha} = 1.54 \text{ \AA}$), θ is position of diffraction peak and (h, k, l) is Miller indices (in this case $(h, k, l) = (0, 0, 4)$). Then from lattice constant, concentration of Mn and Al can be estimated. In case of GaMnAs, Mn concentration can be estimated by typical Vegard's law as shown below;

$$a_{\text{Ga}_{1-x}\text{Mn}_x\text{As}} = a_{\text{GaAs}} \cdot (1 - x) + a_{\text{MnAs}} \cdot x \quad (3.2.1.2)$$

where $a_{\text{Ga}_{1-x}\text{Mn}_x\text{As}}$, a_{GaAs} , a_{MnAs} are lattice constant for GaMnAs (measured), GaAs and MnAs, respectively and x is Mn concentration [74]. However, in case of AlGaAs, linear approximation in Vegard's law is not sufficiently accurate, so additional nonlinear bowing effect must be taken into account as below;

$$a_{\text{Al}_x\text{Ga}_{1-x}\text{As}} = a_{\text{GaAs}} \cdot (1 - x) + a_{\text{AlAs}} \cdot x + x(1 - x)c \quad (3.2.1.3)$$

where $a_{\text{Al}_x\text{Ga}_{1-x}\text{As}}$, a_{GaAs} , a_{AlAs} are lattice constant for AlGaAs (measured), GaAs and AlAs, respectively, x is Al concentration and c is bowing parameter ($c=1.245 \times 10^{-3} \text{ \AA}$) [70]. Mn and Al concentration estimated from θ - 2θ scan to be ~6% and ~75%.

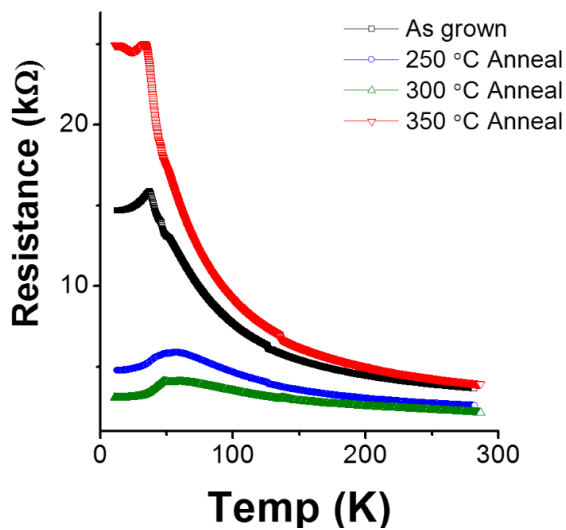


Figure 3.5 Resistance vs. temperature plot for different post-annealing temperatures.

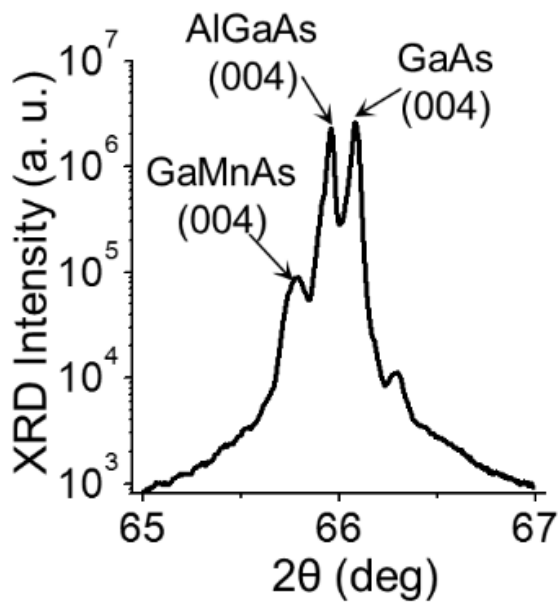


Figure 3.6 High resolution X-ray diffraction (HR-XRD) θ - 2θ scan of sample [72].

3.3 Fabrication of freely-suspended GaMnAs structures

3.3.1 Motivation of freely-suspended structure

Fabrication of freely-suspended structure inevitably involves etching of sacrificial layer underneath the structure. Since MBE growth process is a typical pseudomorphic process and both AlGaAs and GaAs owns lattice constant greater than GaMnAs, GaMnAs layer grown on GaAs/AlGaAs is inevitably under compressive strain due to lattice-mismatch. Prior to this research, suspended structures were fabricated using similar technique which will be described later. However, all structures showed buckling behavior after sacrificial layer etch process, as shown in figure 3.7. This buckling behavior after sacrificial layer etch which removes AlGaAs underneath Hall bar structure is attributed to compressive stress applied along its axis and is a result of lattice-mismatch between GaMnAs and AlGaAs in which causes a compressive strain of $\sim 0.2\%$. In order to verify this buckling of suspended structure, cross-like structures were fabrication and scanning electron microscope image of the structures were taken before and after sacrificial layer etch process. As shown in figure 3.8, GaMnAs structures do not show any sign of buckling before sacrificial layer (AlGaAs) etch process. However, after sacrificial layer etch process, these structures buckled.

Buckling of Hall bar structures are significant obstacle in the analysis of magnetization detection via electrical measurement. In the study of magnetization in a structure, Stoner-Wohlfarth model (SW model) which consider the structure as a

single magnet is widely used. In SW model, angles among current, magnetization and applied field are critical variables which determine the free energy of the structure. However, if a structure is buckled, these angles are no longer consistent throughout the structure. Therefore, a relaxation of strain in the GaMnAs structure without buckling of the structure is essential to analysis of magnetization changes in the structure.

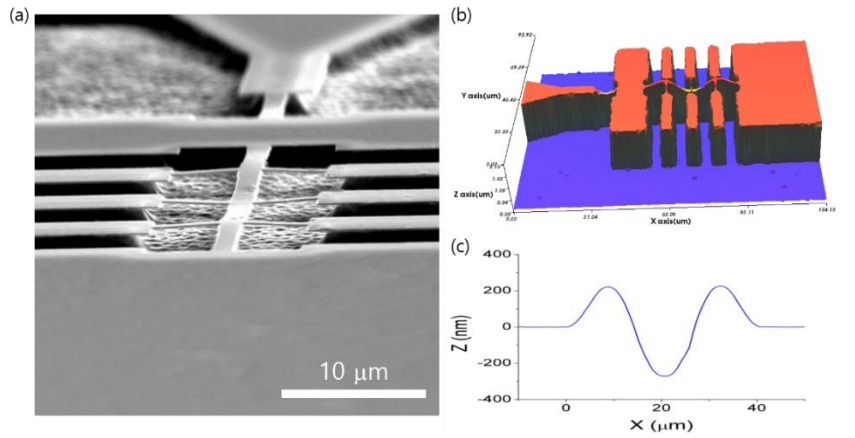


Figure 3.7 (a) SEM image of GaMnAs Hall bar structure after sacrificial layer etch. (b) non-contact optical profiler image of buckled Hall bar. (c) cross-sectional (along main axis) morphology extracted from optical profiler image.

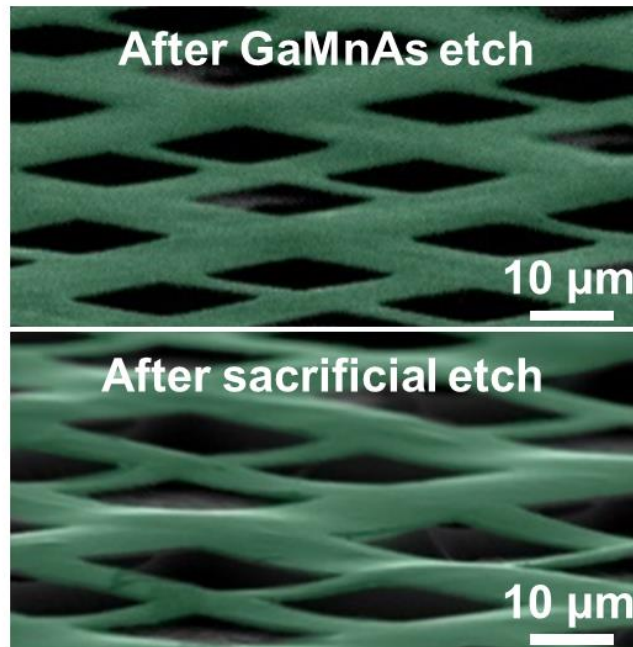


Figure 3.8 GaMnAs cross-like structures before (top) and after (bottom) sacrificial layer etch [72].

3.3.2 Overview of the fabrication process

Fabrication of freely-suspended structures without significant buckling is achieved by incorporation of metallic leads. In the process of suspending GaMnAs layer, when AlGaAs layer underneath GaMnAs layer is removed, suspended structure which was under compressive strain buckles. Figure 3.8 shows SEM images of cross-like GaMnAs structures before and after sacrificial layers. Buckling of GaMnAs structure causes a significant problem in the process of analyzing the magnetization changes; since each segment of buckled structure own different angle between applied field and the structure, the electrical signal such Hall effect signal becomes average value of each segment, preventing precise analysis of magnetization changes. Therefore, fabrication of free-standing structure requires local relaxation of existing compressive strain in the GaMnAs layer without significant buckling. Incorporation of metallic leads without GaMnAs underneath provide an efficient way to prevent this buckling. As shown in Figure 3.7, if suspended structure is connected to environment by GaMnAs layer, strain in GaMnAs layer has no ‘buffer zone’ within the plane where strain can be relaxed, resulting out-of-plane deformation. Incorporation of metallic leads can isolate the GaMnAs structures and provide ‘buffer zone’ for strain relaxation.

Fabrication of freely-suspended structures with metallic lead supports consists of e-beam lithography, metal deposition, selective chemical etching, undercut etching and critical point drying. In this work two methods have been utilized for fabrication; electrode-deposition-first method and structure-definition-first method. Difference between two methods is in the removal process of GaAs

underneath metallic lead. In the electrode-deposition-first method, metallic electrical leads are achieved first and the GaMnAs underneath metallic leads are removed via undercut chemical etching. On the contrary, later process defines the GaMnAs structures and isolates the structure from the environment by chemical etching which is followed by deposition of metallic leads. Figure 3.9 illustrated the sequence of both fabrication process. In both process, definition of GaMnAs structures were conducted by e-beam lithography and a citric acid/hydrogen peroxide etch at a volume ratio of 7:2 (etch rate: ~200 nm/min) [76]. In the electrode-deposition-first method, the etching time and the lithographic patterns were deliberately controlled and modified to ensure that the GaMnAs below the metallic electrical leads was completely removed and the GaMnAs structure was physically isolated. Then, the sample was subjected to a selective sacrificial etch using 10% HF to remove the sacrificial AlGaAs. Finally, the critical point drying method was applied. In addition to the free-standing GaMnAs structures, control structures of GaMnAs/AlGaAs were also prepared using the same nanomachining process, protected with e-beam resist during the AlGaAs etch.

3.3.3 Fabrication : electrode-deposition-first method

For electrode-deposition-first method, electrical lead as well as contact pad consist of Au (90nm)/ Cr (10 nm) was first deposited on the GaMnAs/GaAs/AlGaAs/GaAs film. The thickness of the metal electrode are carefully selected so that the electrodes can act as soft metallic supports which can

withstand the free-standing structure. Electrical leads are fabricated by standard e-beam lithography. First, polymethyl methacrylate, with molecular weight of 950,000 and diluted in anisol with concentration of 4% (PMMA 950K A4), was spin-coated in 4000 RPM for 90 seconds and bake at 180°C for 90 sec. Since this spin-coating process provide ~ 200 nm thick PMMA resist layer, spin-coating process has been repeated twice for resist layer with thickness of ~ 400 nm. This repetition of spin-coating ensures successful lift-off process: it is experimentally known that thickness of resist layer needs to be at least 3 times thicker than the materials to be deposited. E-beam lithography was conducted using 30 keV thermal scanning electron microscope (SEM) equipped with nanometer pattern generation system (NPGS). Then, the exposed patterns were developed using methyl isobutyl ketone (MIBK) : isopropyl alcohol (IPA) = 1:3 solution for 60 seconds in room temperature. Au (90nm)/ Cr (10 nm) metal electrodes were deposited using e-beam evaporation with base pressure ~ 1.0×10^{-6} Torr, followed by lift-off process using acetone with sonic agitation if necessary.

After electrodes fabrication, PMMA mask for GaMnAs structure was fabricated using e-beam lithography similar to the one mention above, but this time with only one layer of PMMA spin-coated. Unlike electrode fabrication which electrode area is exposed to electron beam, the area around the structure is exposed to electron beam in PMMA masking fabrication so that the PMMA mask protects GaMnAs structure while etching process. Then, GaMnAs etching was conducted using a citric acid/hydrogen peroxide etch at a volume ratio of 7:2 (etch rate: ~200 nm/min) [76]. During the etching of the GaMnAs, the etching time and the

lithographic patterns were deliberately controlled to ensure that the GaMnAs below the metallic electrical leads was completely removed and the GaMnAs structure was physically isolated. Then, PMMA layer was removed by acetone and sacrificial etching window was fabrication using PMMA masking and e-beam lithography. Since our goals was to fabricate the free-standing GaMnAs structures and control structures of GaMnAs/AlGaAs, or unsuspended structures, on the same sample, PMMA layer on control structures area were not exposed to electron beam so that the structures are protected during the AlGaAs etch. Then the sample was subjected to a selective sacrificial etch using 10% HF to remove the sacrificial AlGaAs [77]. Finally, the critical point drying method was applied after removal of PMMA layer using acetone. Usage of critical point drying prevents collapse of suspended structure during drying process, utilizing continuity of state for which there is no apparent difference between the liquid and gas state of a medium where the surface tension between this interface reducing to zero [78].

Electrode-deposition-first method demands fewer steps in fabrication process. However, this method requires delicate control of etching time as well as the lithographic patterns in order to remove the GaMnAs layer underneath metallic electrical lead supports completely. Since this process involves undercut etching underneath metallic lead which utilizes the lateral etching, failure of etching control results unrecoverable damage to the suspended structures and mostly ends up with collapse of the structures.

3.3.4 Fabrication : structure-definition-first method

Structure-definition-first method was developed in order to resolve the problems in electrode-deposition-first method which result in collapse of the structures. Instead of using undercut-based etching process, this process defines the GaMnAs structures first, followed by metal deposition. First, using e-beam lithography, as mentioned above, PMMA masks for GaMnAs structures are fabricated using identical spin-coating and developing condition as described earlier. Then, GaMnAs etching was conducted using a citric acid/hydrogen peroxide etch at a volume ratio of 7:2. Again, using e-beam lithography metallic electrical leads are fabricated and Au (100 nm)/ Cr (80 nm) was deposited. The thickness of the metallic layer is chosen so that the deposited metal covers the step-edge at the end of the GaMnAs structure from GaMnAs etch. Then, identical sacrificial layer etch process is conducted, followed by critical point drying.

Structure-definition-first method, by depositing metal layer after GaMnAs etching process, does not requires undercut-based GaMnAs etch, ensuring stable GaMnAs etching condition. Furthermore, since GaMnAs layer is etched based on vertical etch, lithographical patterns are much easier to design: structure design no longer requires significant consideration of lateral etch rate. On the other hand, this process requires additional step in the fabrication process.

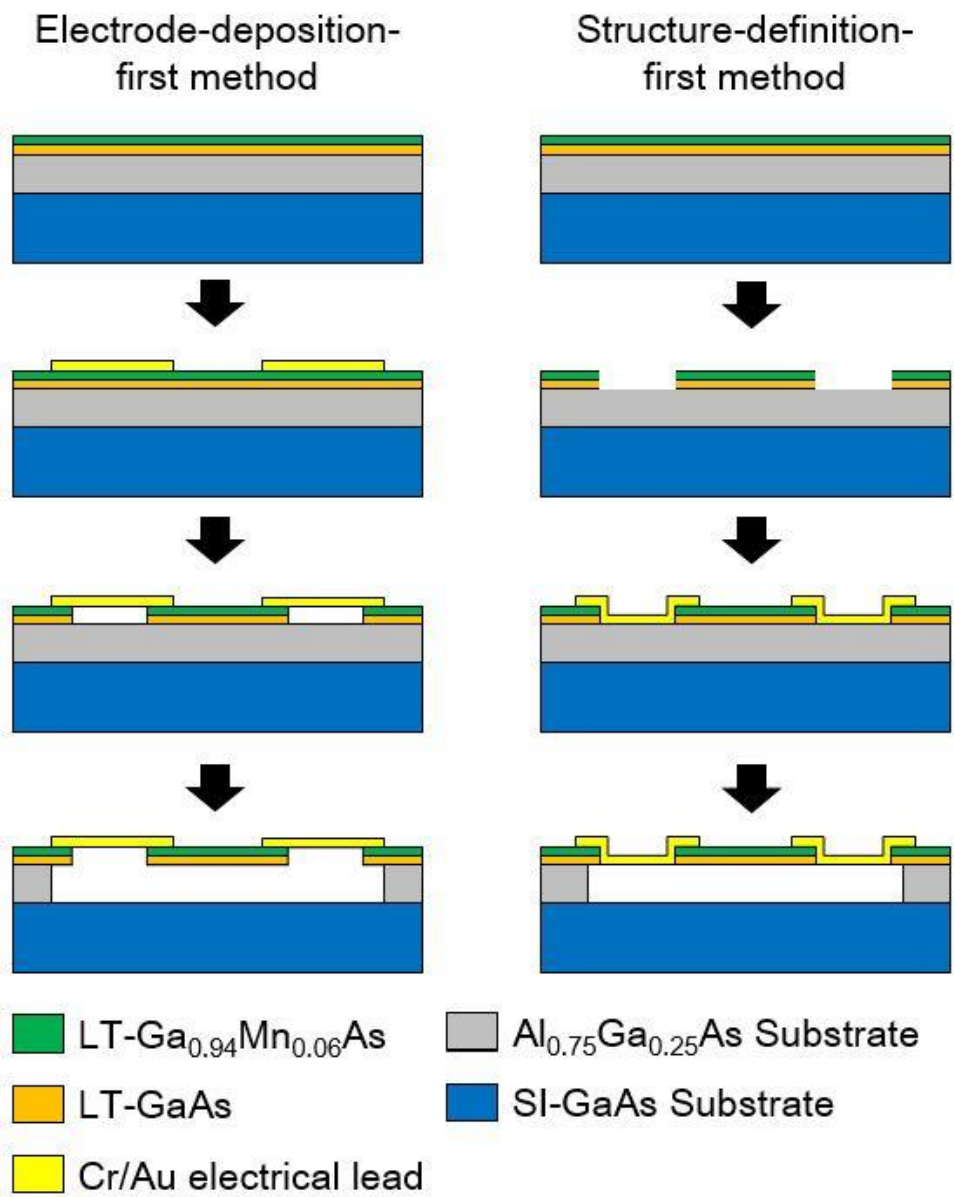


Figure 3.9 Schematics of fabrication processes

(Blank page)

4 Anomalous Hall effect measurements in freely-suspended GaMnAs microsheet in van der Pauw geometry

In this chapter, Anomalous Hall effect measurement conducted in freely-suspended GaMnAs microsheet in van der Pauw geometry will be discussed.

4.1 Sample preparation and measurement set-up

As introduced in Chapter 3, freely-suspended $10\ \mu\text{m} \times 10\ \mu\text{m}$ GaMnAs nanosheet were fabricated using electrode-deposition-first method. All samples were prepared in which both suspended structure and unsuspended structure are achieved in a single substrate. For measurement of anomalous Hall effect, sample was mounted commercially available closed-cycle magnetocryostat (IceOxford ^{DRY}ICE⁴ ^{TL}, ICE Oxford Ltd., Witney, UK) using the standard AC lock-in transport technique ($I = 0.1\ \mu\text{A}$ at 17 Hz and 23 Hz). Measurements for both suspended structure and unsuspended structure are conducted simultaneously using two different AC frequency as mentioned above. SEM image of achieved microsheet are illustrated in Figure 4.1, which clearly shows no sign of buckling.

4.2 Temperature dependent longitudinal resistivity

Prior to magnetoresistance measurement, temperature dependent longitudinal resistivity of both suspended and unsuspended sample were measured. As shown in Figure 4.2, both suspended and unsuspended sample exhibited clear metallic behavior and a temperature-dependence anomaly corresponding to $T_C \sim 85$ K. For both suspended and unsuspended GaMnAs structure, $\rho_{xx} < 10$ m Ω ·cm; this resistivity is consistent with GaMnAs exhibiting an intrinsic AHE [26]. Furthermore, differential resistivity ($d\rho_{xx}/dT$) for both structure shows almost identical behaviors which suggests that suspending fabrication process does not alter macroscopic characteristics of GaMnAs layers.

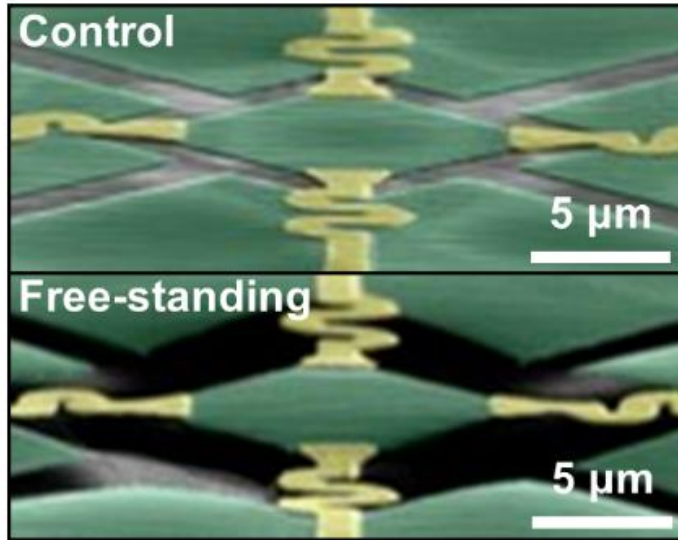


Figure 4.1 SEM image of control (**top**) and free-standing (**bottom**) van der Pauw structures with added false color to distinguish the GaMnAs layer (green) and electrical leads (gold) [72].

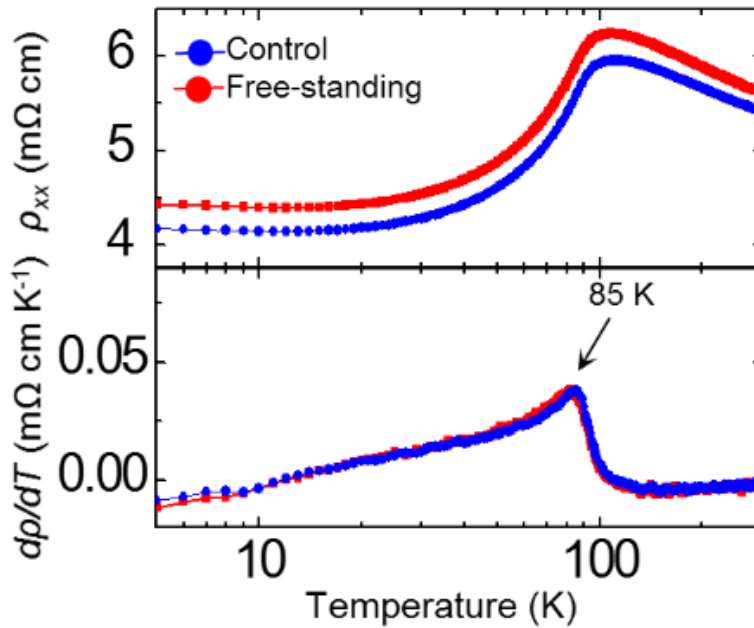


Figure 4.2 Temperature-dependent resistivity (ρ_{xx} vs. T) and the corresponding differential resistivity ($d\rho_{xx}/dT$) [72].

4.3 Finite-element analysis of GaMnAs microsheet

Although the electrical leads were symmetrically patterned with a serpentine geometry to minimize any thermally induced strain, because of the large difference between the coefficient of thermal expansion of GaMnAs and that of the metallic electrical leads, we could not fully eliminate such thermoelastic/piezoresistive effects, which may have served as a source of the slight discrepancy between the temperature dependences of the resistivities of the two structures. We attempted to quantify the thermally induced strain using a commercially available finite-element analysis package (COMSOL Multiphysics 4.3b, COMSOL Inc., Burlington, USA). Figure 4.3 summarizes the results of the finite-element analysis by mapping the expected stress for the control GaMnAs/GaAs/AlGaAs structure and the free-standing GaMnAs microsheet structure anchored by serpentine-shaped metallic leads at the corners for 300 K and 10 K. At $T = 10$ K, much of the stress is limited to the sections with the leads, as expected. On the free-standing GaMnAs sheet, the stress is nearly uniform, and areas of high stress are limited to the regions where the metallic leads clamp the corners of the sheet (with a maximum stress value of ~ 400 MPa, which rapidly falls to < 100 MPa within 100 nm from the edge). Using the Young's modulus of GaAs, which is 86 GPa, we can estimate the effective strains to be less than 0.001 at 10 K, which we expect to have minimal effects on ρ_{xx} and ρ_{xy} [79].

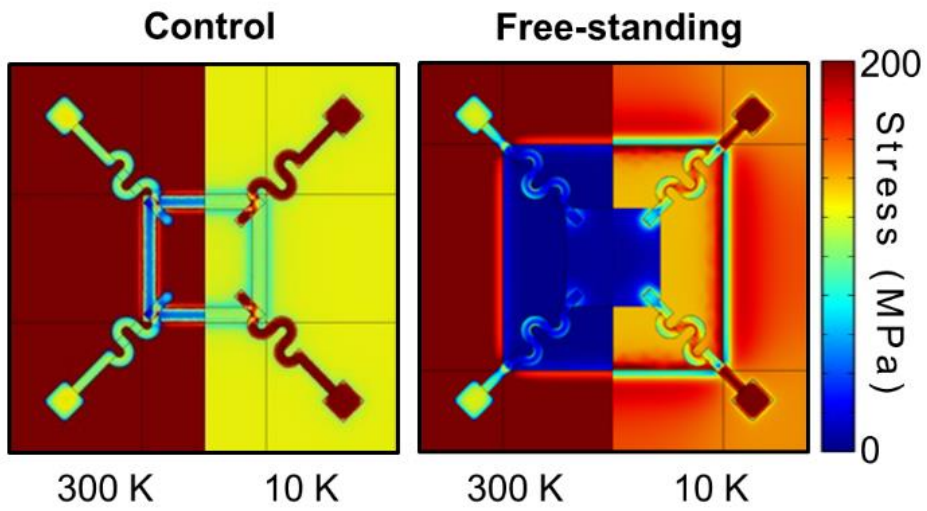


Figure 4.3 Finite-element analysis mapping the calculated stress distributions for the control and free-standing GaMnAs microsheets for $T = 300\text{ K}$ and 10 K [72].

4.4 Magnetoresistance measurement in freely-suspended GaMnAs microsheets.

Magnetotransport measurements were performed to simultaneously measure ρ_{xx} and ρ_{xy} with an applied magnetic field perpendicular to the free-standing GaMnAs microsHEET ($H < \pm 9$ T) using the AC lock-in measurement technique ($I = 0.1 \mu\text{A}$ at 17 Hz and 23 Hz). Figure 4.4(a) plots the longitudinal resistance as a function of the applied magnetic field at $T = 10$ K. The low-field response ($H < \pm 1$ T) shows similar absolute resistance changes for both the free-standing GaMnAs and the control. The switching characteristics, however, show marked differences: the magnetization of the free-standing GaMnAs flips at much lower fields. Figure 4.4(b) plots the transverse resistance as a function of the applied magnetic field at $T = 10$ K. As implied by the AMR response presented in Figure 4.4(a), the Hall response also suggests that the easy magnetization direction is more in-plane-like for the control sample and more out-of-plane-like for the free-standing GaMnAs microsHEET. Beyond GaMnAs, similar effects have been reported in metallic magnetic thin films in which the magnetic anisotropy was varied by applying strain to a flexible substrate [80]. Such changes in the GaMnAs magnetic anisotropy warrant a further detailed study by means of planar Hall effect measurements. Figure 4.4(c) plots the transverse resistance as a function of the applied field at temperature of 10 K, 50 K, and 100 K. At temperatures below T_C , the Hall response from the free-standing sample suggests a stronger Hall effect contribution from spontaneous magnetization, which is ascribed to the more out-of-plane-like easy magnetization direction. For both samples, a

remnant AHE is readily seen above T_C . This remnant AHE is due to residual spontaneous magnetization, which is ascribed to the second-order transition (or continuous transition) from ferromagnetism to paramagnetism.

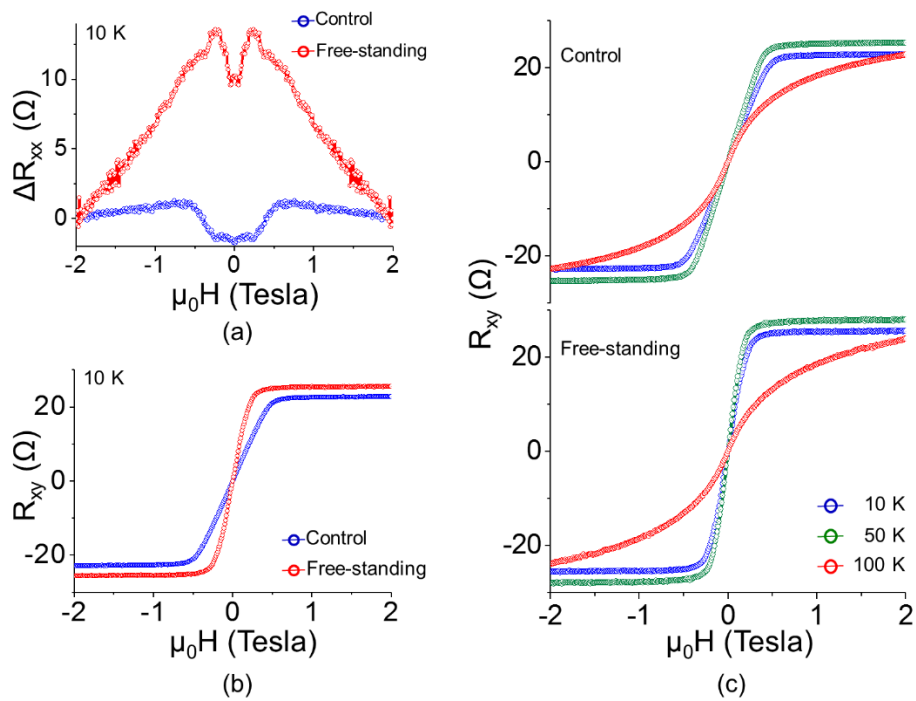


Figure 4.4 . **(a)** Longitudinal Hall resistance as a function of the applied magnetic field (ΔR_{xx} vs. H) at $T = 10$ K. **(b)** Transverse Hall resistance as a function of the applied magnetic field (R_{xy} vs. H) at $T = 10$ K. **(c)** Field-dependent transverse Hall resistance (R_{xy} vs. H) at various temperatures [72].

4.5 Summary

Anomalous Hall effect responses in suspended GaMnAs nanosheets suggests that by relaxing built-in strain in GaMnAs layer, easy magnetization direction of GaMnAs nanostructure can be altered from in-plane-like to more out-of-plane-like. Both SEM image and FEA analysis suggests no sign of significant buckling has been occurred in the process of suspension which appears in no significant changes in microscopic characteristics (both ρ_{xx} vs. T and $d\rho_{xx}/dT$). However, due to the geometry of the van der Pauw, mixing between signal from ρ_{xx} and ρ_{xy} occurred: in the AHE measurement this mixing could be removed using parity, but in PHE measurement parity method is no longer valid. In order to further analyze the change in magnetization via strain relaxation, planar Hall effect measurement is essential. Thus, specimen with Hall bar geometry was fabrication and the planar Hall response was measured and will be described in next chapter.

(Blank page)

5 Anomalous and Planar Hall effect measurements in freely-suspended GaMnAs in Hall bar geometry

In this chapter, anomalous and planar Hall effect measurement conducted in freely-suspended GaMnAs nanostructure in Hall bar geometry will be discussed. As mentioned in previous chapter, freely-suspending GaMnAs layer with incorporation of metallic electric leads significantly reduces strain in GaMnAs layer which is built during pseudomorphic MBE-growth, resulting change in easy magnetization direction from in-plane-like to out-of-plane-like. However, for further confirmation of this change in easy magnetization direction as well as analysis of its origin requires further research in in-plane magnetization of freely-suspended structure. Hall bar geometry has advantage over van der Pauw geometry in terms of separating longitudinal and transverse Hall signal.

5.1 Sample preparation and measurement set-up

As introduced in Chapter 3, freely-suspended $6\ \mu\text{m} \times 60\ \mu\text{m}$ GaMnAs Hall bars were fabricated using structure-definition-first method. All samples were prepared in which both suspended structure and unsuspended structure are achieved in a single substrate. For measurement of anomalous Hall effect, sample was mounted commercially available closed-cycle magnetocryostat (IceOxford ^{DRY}ICE⁴™, ICE Oxford Ltd., Witney, UK) using the standard AC lock-in transport technique

($I = 0.1 \mu\text{A}$ at 17 Hz and 23 Hz). Measurements for both suspended structure and unsuspended structure are conducted simultaneously using two different AC frequency as mentioned above. SEM image of achieved microsheet are illustrated in Figure 5.1, which clearly shows no sign of buckling. Minimization of deformation is also confirmed to be less than 100 nm over 60 μm length by non-contact optical profiler measurement as shown in Figure 5.2.

5.2 Finite-element analysis of GaMnAs Hall bar structure

Similar to van der Pauw geometry, quantify the thermally induced strain using a commercially available finite-element analysis package (COMSOL Multiphysics 4.3b, COMSOL Inc., Burlington, USA). Figure 5.3 summarizes the results of the finite-element analysis by mapping the expected stress for the control GaMnAs/GaAs/AlGaAs structure and the free-standing GaMnAs structure anchored by metallic leads at the corners for 300 K and 10 K. At $T = 10 \text{ K}$, much of the stress is limited to the sections with the leads and Hall bar lead for voltage sensing, as expected. On the free-standing GaMnAs structure, the stress is not uniform any more, but still areas of high stress are limited to the regions where the metallic leads clamp the end of the Hall bar (with a maximum stress value of $\sim 400 \text{ MPa}$, which rapidly falls to $< 100 \text{ MPa}$ within 100 nm from the edge) and voltage sensing lead which unlikely effect magnetization of Hall bar.

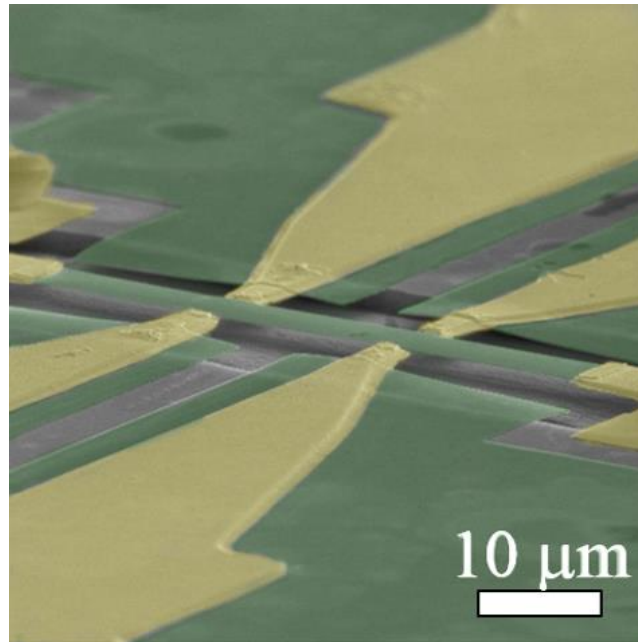


Figure 5.1 SEM image of freely-suspended GaMnAs Hall bar structure

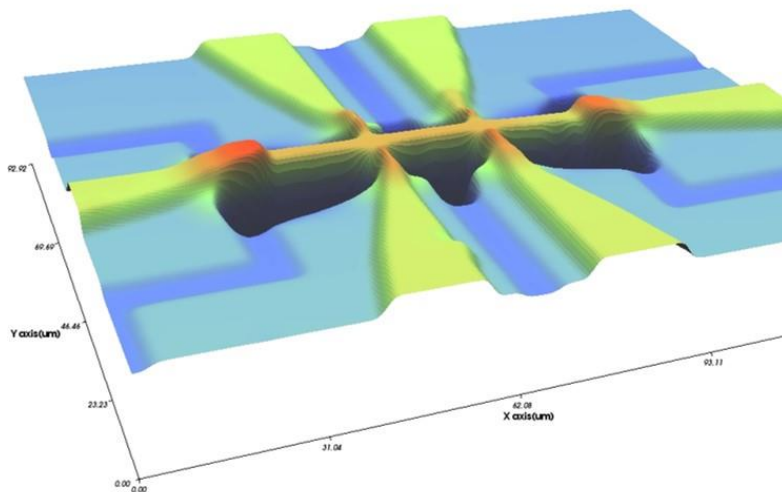


Figure 5.2 Non-contact optical profile image of suspended GaMnAs Hall bar structure

5.3 Angle definition for planar and normal Hall geometry

For the convenience in the following section, magnetization angle (θ_M) as well as applied field angle (θ) in planar Hall geometry need to be defined. As shown in Figure 5.4, magnetization angle (θ_M) is defined as angle between magnetization and current direction which is GaAs [1 1 0] direction, and applied field angle (θ) is defined as angle between applied field and current direction. Both angles are in the x-y plane.

For the same reason, magnetization angle (φ_M) as well as applied field angle (φ) in normal Hall geometry need to be defined. As shown in Figure 5.5, magnetization angle (φ_M) is defined as angle between magnetization and current direction which is GaAs [1 1 0] direction, and applied field angle (φ) is defined as angle between applied field and current direction. Both angles are in the x-z plane.

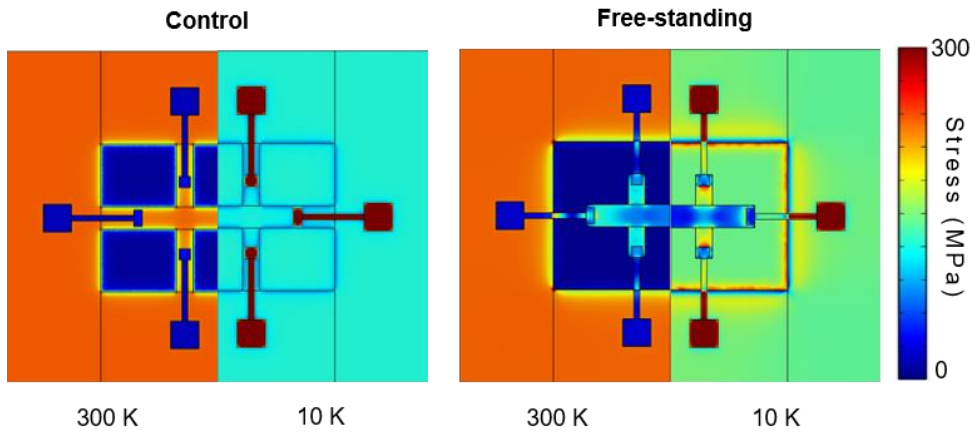


Figure 5.3 Finite-element analysis mapping the calculated stress distributions for the control and free-standing GaMnAs microsheets for $T = 300$ K and 10 K

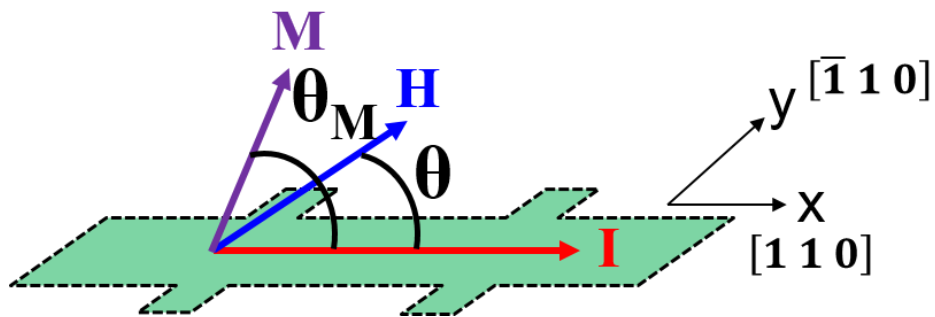


Figure 5.4 Schematic for angle definition for planar Hall geometry.

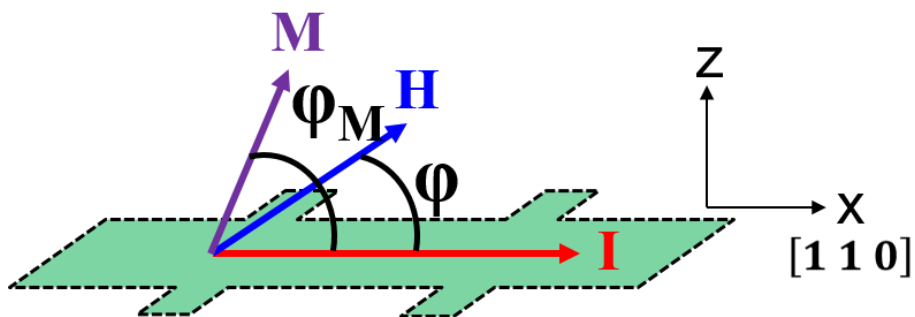


Figure 5.5 Schematic for definition for angle definition for normal Hall geometry.

5.4 Temperature dependent longitudinal resistivity

Again, Prior to magnetoresistance measurement, temperature dependent longitudinal resistivity (ρ_{xx} vs. T) of both suspended and unsuspended sample were measured. As shown in Figure 5.6, both suspended and unsuspended sample exhibited similar behavior and a temperature-dependence anomaly corresponding to $T_C \sim 65$ K, suggests that suspending fabrication process does not alter macroscopic characteristics of GaMnAs layers. Furthermore, it is clear differential resistivity ($d\rho_{xx}/dT$) calculated from ρ_{xx} vs. T for both structure will show almost identical behaviors.

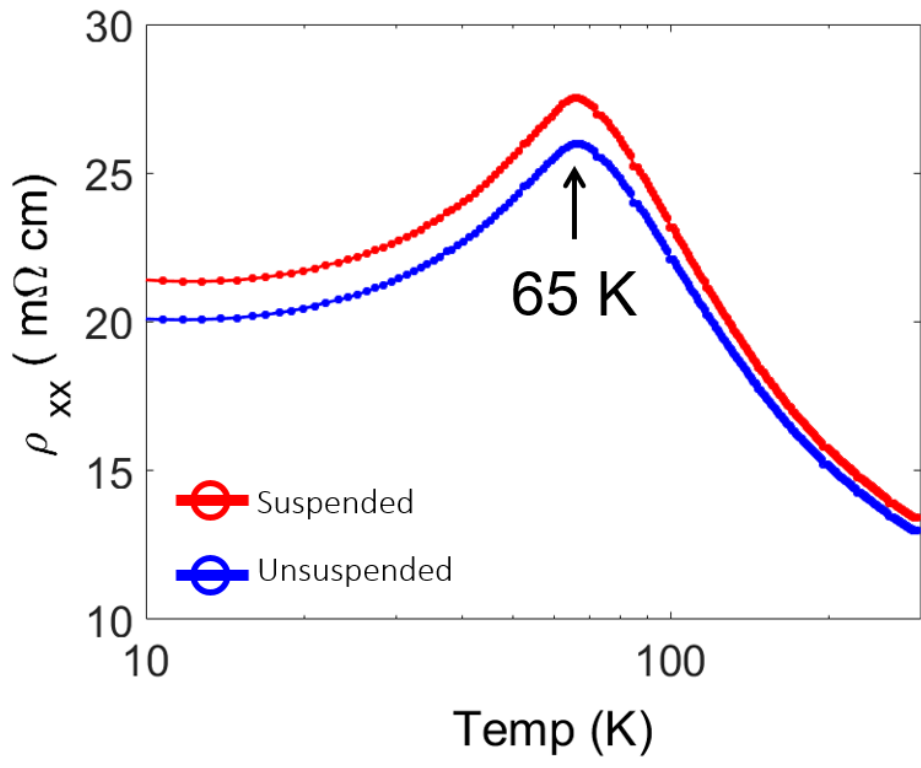


Figure 5.6 Temperature-dependent resistivity (ρ_{xx} vs. T).

5.5 Planar Hall effect measurement of GaMnAs Hall Bar structure

Magnetotransport measurements were performed to simultaneously measure R_{xx} and R_{xy} with an applied magnetic field parallel to the free-standing GaMnAs Hall bar structure, with sample rotating within the plane parallel to applied magnetic field of 1.2 T, using the AC lock-in measurement technique ($I = 0.1 \mu\text{A}$ at 17 Hz and 23 Hz). Figure 5.7 plots the longitudinal resistance as a function of applied field angle (R_{xx} vs. θ) at the temperature of 4 K, 15 K, 30 K, 60 K, and 90 K. From R_{xx} below 30 K, it is depicted that the resistance change in suspended sample is significantly reduced compare to unsuspended sample. This reduction in longitudinal resistance change disappears as temperature passes biaxial to uniaxial transition temperature which is $\sim 30 \text{ K}$ ($T_C/2$). Furthermore, reduction in resistance change appears strongly at the angle which correspond to $[\bar{1} 1 0]$ crystal direction of GaMnAs.

Reduction in resistance change along $[\bar{1} 1 0]$ is depicted much clearly in the polar plot as shown in figure 5.8. Along 90° and 270° which correspond to $[\bar{1} 1 0]$ of GaMnAs, significant dent in longitudinal resistance clearly appears for unsuspended GaMnAs structure at temperature below 30 K. However, in suspended GaMnAs structure, this dent in longitudinal resistance appears only at 4 K with significantly reduced magnitude and disappears at other temperature.

This reduction in resistance change along $[\bar{1} 1 0]$ can be explained by reduction in biaxial in-plane magnetic anisotropy. Since applied field is 1.2 T which is much stronger than coercive field of GaMnAs ($< \text{few thousand Oersted}$),

magnetization of GaMnAs structure can be described by Stoner-Wohlfarth model as mentioned in chapter 2. Reduction of in biaxial in-plane magnetic anisotropy implies lowering of the energy barrier between each magnetization biaxial easy axis. Since longitudinal resistance change strongly depends on height of these energy barrier, reduction of these energy barrier result in reduction in longitudinal resistance change. As temperature increase above $\sim T_C/2$, biaxial magnetic anisotropy disappears as mentioned earlier and thus this reduction in longitudinal resistance change also disappears.

Reduction in biaxial in-plane magnetic anisotropy was revealed more evidently in transverse resistance. Figure 5.9 shows transverse resistance as a function of applied field angle (R_{xy} vs. θ) at the temperature of 15 K with applied field of 200 Oe, 500 Oe, 1500 Oe and 12000 Oe. At applied field at and below 500 Oe, unsuspended GaMnAs structure clearly shows switching behavior. This anomalous switching behaviors of transverse Hall resistance are attributed to a two jump sequence of magnetization: $[1\ 0\ 0]$ ($\theta_M \sim -45^\circ$) \rightarrow $[0\ 1\ 0]$ ($\theta_M \sim 45^\circ$) \rightarrow $[\bar{1}\ 1\ 0]$ ($\theta_M \sim 135^\circ$) [81]. However, in case of suspended GaMnAs structure, this Hall resistance jumping behavior disappear: transverse Hall resistance rather follows semi-sinusoidal shape. Again, this anomalous transverse Hall resistance jumping behavior disappears at applied field above 1500 Oe. Figure 5.10 illustrates transverse Hall resistance a function of applied field angle (R_{xy} vs. θ) in a polar plot. Resistance jumping behavior in unsuspended GaMnAs structure appears as a sharp transition in the plot where suspended GaMnAs do not show any of this sharp transition.

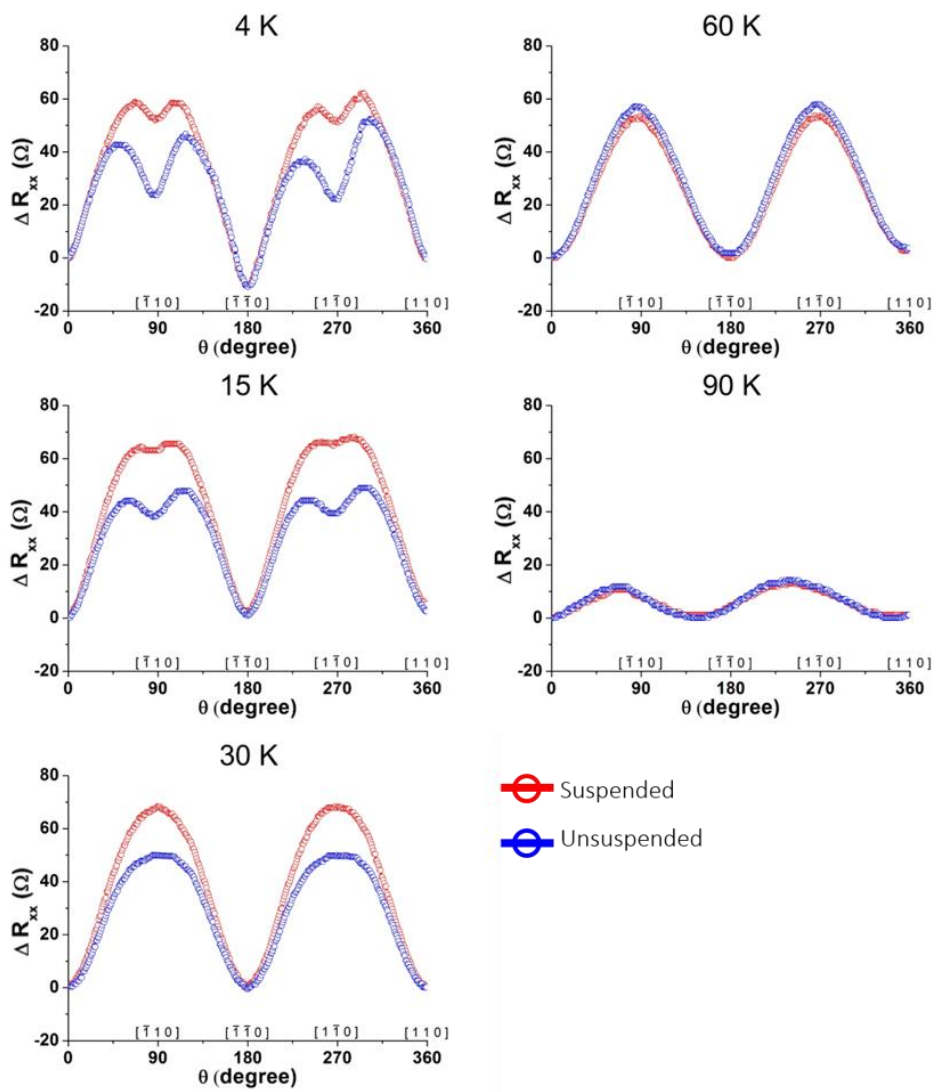


Figure 5.7 Longitudinal resistance as a function of applied field angle (R_{xx} vs. θ) at the temperature of 4 K, 15 K, 30 K, 60 K, and 90 K.

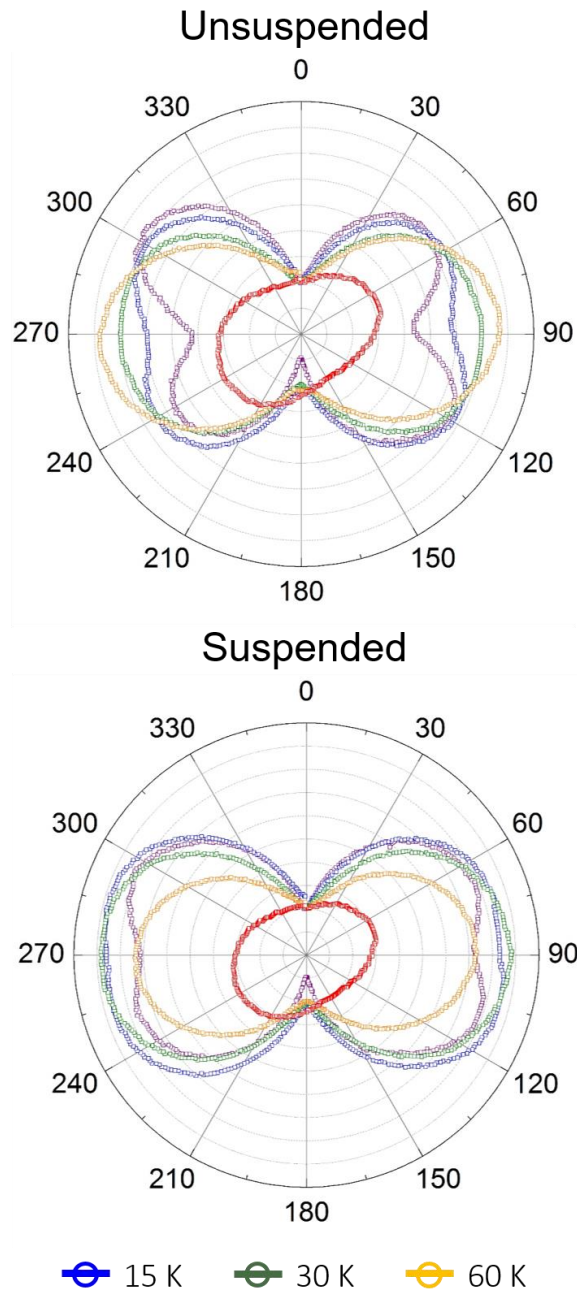


Figure 5.8 Polar plot of longitudinal resistance as a function of applied field angle (R_{xx} vs. θ) at the temperature of 4 K, 15 K, 30 K, 60 K, and 90 K.

Lose of transverse Hall resistance jumping behavior implies modification in in-plane magnetic anisotropy. As mentioned earlier, switching behaviors of transverse Hall resistance are attributed to a two jump sequence of magnetization. With easy magnetization axis lying at the x-y plane shown in Figure 5.4, magnetization at low applied field (< 500 Oe) must lie collinear to the magnetic easy axis which correspond to biaxial magnetic anisotropy. As a result, for the case of unsuspended structure, magnetization tend to stay collinear with each magnetic easy axis ($\sim 45^\circ$, $\sim 135^\circ$, $\sim 225^\circ$, $\sim 315^\circ$). Again, between each magnetic easy axis, there are energy barriers from magnetic anisotropy which prevent magnetization reversal at applied field below coercive field. According to Stoner-Wohlfarth model, magnetization can be reverse from an easy axis (M_i) to next easy axis (M_f) requires characteristic pinning energy density (ε) as below;

$$\varepsilon > H_C \cdot (M_f - M_i) \quad (5.5.1)$$

where H_C is coercive field and determined by magnetic anisotropy energy. If in-plane magnetic anisotropy is reduced by certain mean, value of coercive field can be changed. Thus, in this case, if suspending GaMnAs structure reduced in-plane magnetic anisotropy, coercive field value is also reduced. According to (5.5.1), with significantly reduced coercive field, magnetization no longer jump switch between easy axis, but will rotate coherently with applied field as shown in transverse Hall resistance of suspended GaMnAs structure.

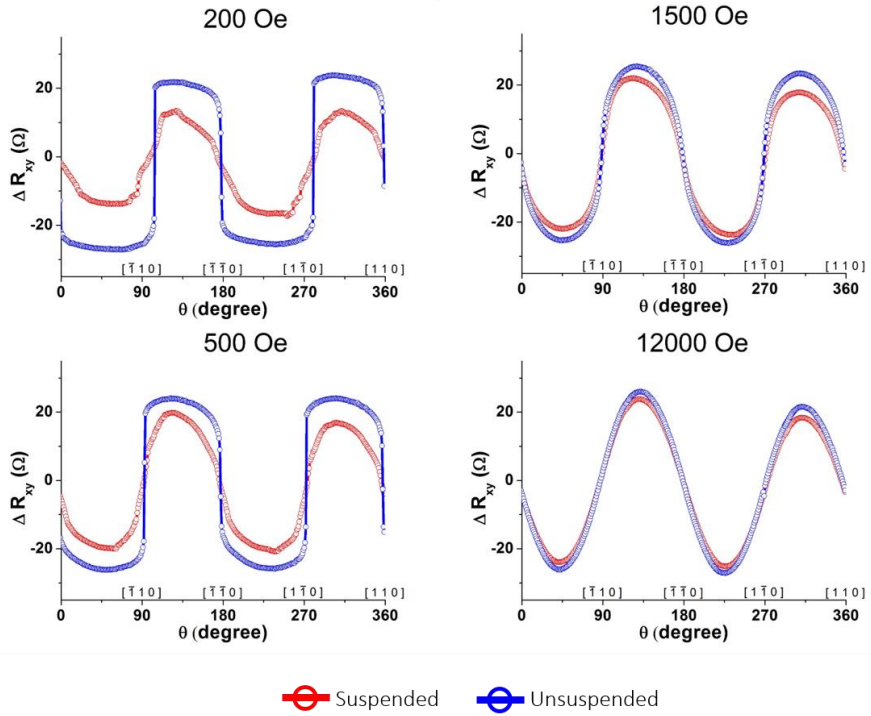


Figure 5.9 Transverse resistance as a function of applied field angle (R_{xx} vs. θ) at the temperature of 15 K and applied field of 200 Oe, 500 Oe, 1500 Oe and 12000 Oe.

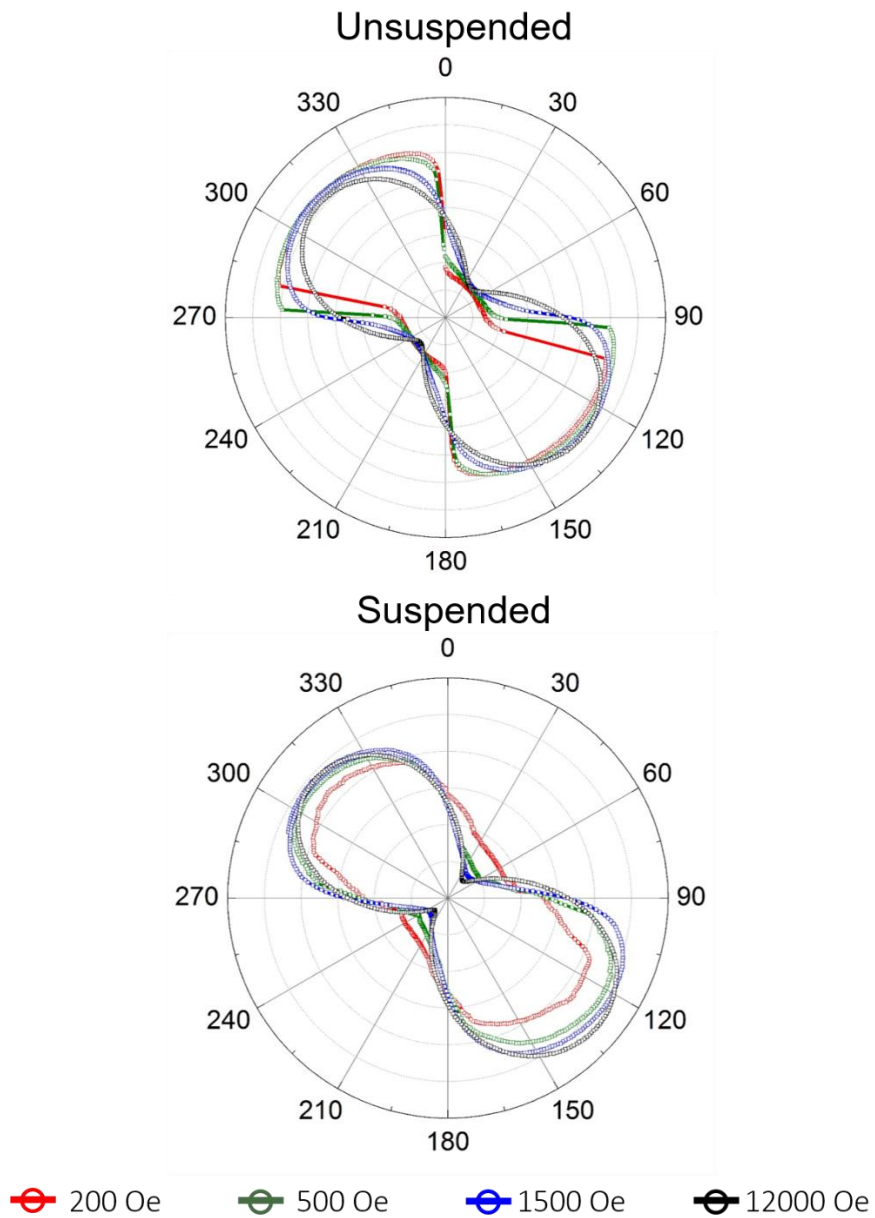


Figure 5.10 Polar plot of transverse resistance as a function of applied field angle (R_{xx} vs. θ) at the temperature of 15 K and applied field of 200 Oe, 500 Oe, 1500 Oe and 12000 Oe.

The longitudinal planar Hall response can be explained by Stoner-Wohlfarth model for longitudinal electrical field which is given in Eq. (2.3.1) as shown below:

$$E_x = j\rho_{\perp} + j(\rho_{\parallel} - \rho_{\perp}) \cos^2 \theta_M \quad (2.3.1).$$

The longitudinal electrical field has two component of resistivity perpendicular to magnetization (ρ_{\perp}) and the difference between resistivity parallel and perpendicular to magnetization ($\rho_{\parallel} - \rho_{\perp}$). Since the former term only gives offset value to the longitudinal planar Hall response, the shape of the longitudinal planar Hall response is determined by the value of $\rho_{\parallel} - \rho_{\perp}$, more specifically the sign of $\rho_{\parallel} - \rho_{\perp}$. The sign of $\rho_{\parallel} - \rho_{\perp}$ can be deduced from the transverse planar Hall response which is shown in Fig. 5.9 and the Eq. (2.3.2) shown below:

$$E_y = j(\rho_{\parallel} - \rho_{\perp}) \sin \theta_M \cos \theta_M \quad (2.3.2).$$

Since the transverse planar Hall response exhibits first maxima at $\sim 135^\circ$ instead of $\sim 45^\circ$, it is evident that the value of $\rho_{\parallel} - \rho_{\perp}$ is negative, indicating $\rho_{\parallel} < \rho_{\perp}$. This property of GaMnAs is distinct from that in conventional ferromagnetic metal, where $\rho_{\parallel} > \rho_{\perp}$. This different behavior in resistivity is attributed to combined

effect of the SO-coupled spin-texture in the host band and polarized scatterers containing nonmagnetic and magnetic impurity potentials which is discussed earlier in Eq. (2.2.2). In other words, difference in the ratio of nonmagnetic and magnetic parts of the impurity potential resulted in the minima at the $\sim 0^\circ$ and $\sim 180^\circ$ which is normally maxima in conventional ferromagnetic metals [78]. In addition, the imperfection of symmetry in Fig. 5.8 can be attributed to the misplacement of the sample on the sample holder which is estimated to be less than 5° . This error are inevitable in our measurement system, since the axis of the sample holder is fix relative to the orientation of the magnet. Application of vector field magnet, which can rotate the orientation of the magnetic field freely, can be the solution for this type of errors.

In the transverse planar Hall resistance, application of Stoner-Wohlfarth model mainly concerned the terms related to the uniaxial and biaxial magnetic anisotropy. In order to prevent mixture of signal from these anisotropies with signal from shape anisotropy, the fabricated GaMnAs structure has main axis (length direction) along the $[1\ 1\ 0]$ direction so that the terms concerning shape anisotropy can be included in the uniaxial anisotropy term. This selection of the main axis direction aimed to coincide the main axis of the GaMnAs structure to the main axis in the Stoner-Wohlfarth model. Furthermore, the ratio of length and the width of the structure, which correspond to the dimensional ratio, is ~ 10 and as mentioned earlier in 2.2.3, the demagnetizing factor converges to zero as the dimensional ratio increases. Thus, effect is shape anisotropy is small enough and inclusion of shape anisotropy in the uniaxial anisotropy terms is sufficiently valid.

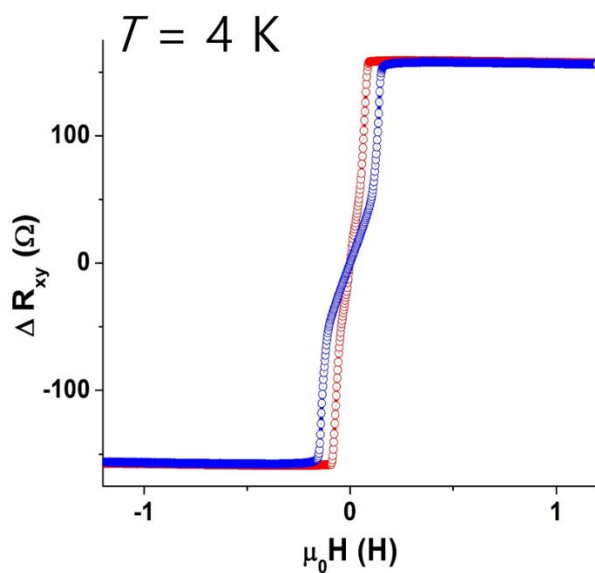
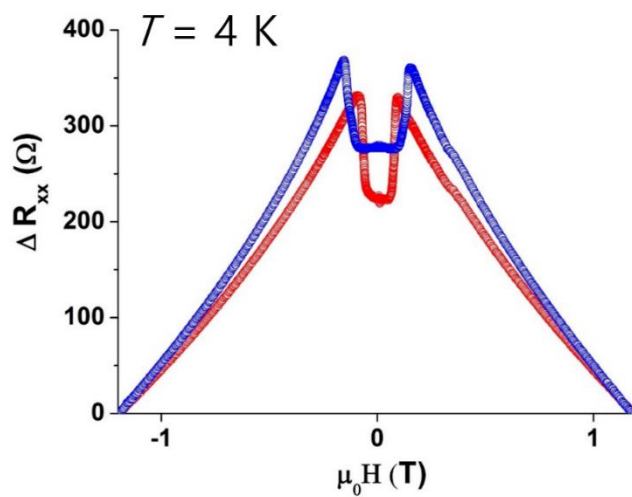
5.6 Anomalous Hall effect measurement of GaMnAs Hall

Bar structure

In order to confirm the reduction of in-plane magnetic anisotropy, magnetotransport measurements were performed to simultaneously measure R_{xx} and R_{xy} with an applied magnetic field perpendicular to the free-standing GaMnAs Hall bar structure, using the AC lock-in measurement technique ($I = 0.1 \mu\text{A}$ at 17 Hz and 23 Hz). Figure 5.11 plots the both longitudinal and transverse Hall resistance as a function of applied field (R_{xx} vs. H , R_{xy} vs. H) at the temperature of 4 K. Transverse Hall resistance of suspended GaMnAs Hall bar structure shows similar behavior to the one from van der Pauw structure which is depicted in figure 4.4. Suspended structure shows smaller coercive field compare to unsuspended structure in R_{xx} vs. H . At the same time, stronger anomalous Hall response from the free-standing sample suggests a stronger Hall effect contribution from spontaneous magnetization, which is ascribed to the more out-of-plane-like easy magnetization direction.

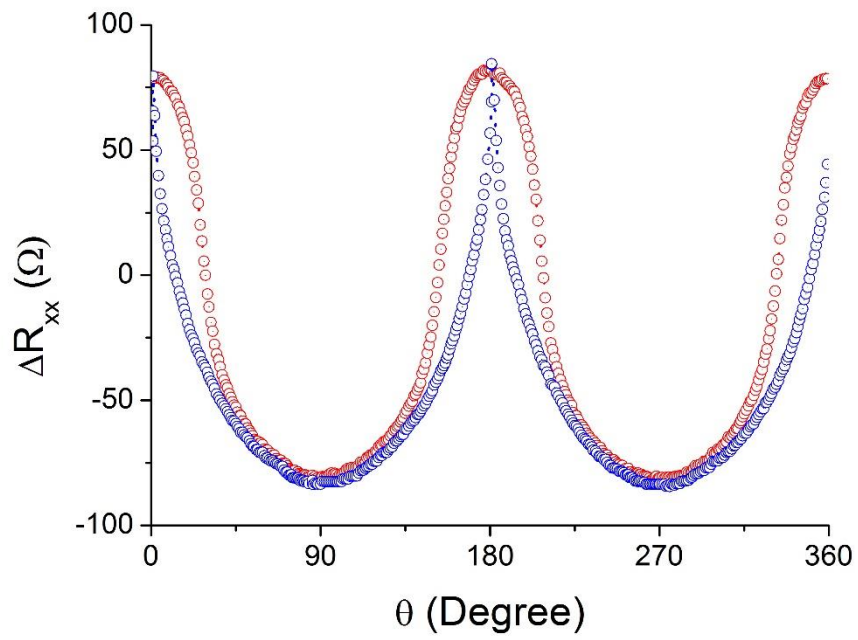
Further investigation of this modification of magnetic anisotropy has been conducted from longitudinal resistance as a function of applied field angle (R_{xx} vs. φ). Figure 5.12 shows longitudinal resistance as a function of applied field angle (R_{xx} vs. φ) at temperature of 4 K and applied field 1500 Oe. In case of unsuspended structure, longitudinal resistance shows typical hard axis response which resistance increase rapidly around 180° where magnetization reversal occurs. However, in case of suspended structure, longitudinal resistance shows a sinusoidal behavior which resistance increase around 180° is not as rapid as unsuspended structure.

This difference in longitudinal resistance can be attributed to modification of out-of-plane magnetic anisotropy. Unsuspended GaMnAs structure which still owns easy magnetization direction parallel to in-plane has a magnetic hard axis along z-axis (vertical axis from sample plane). As a result, sharp transition occurs in longitudinal resistance. On the contrary, in the suspended GaMnAs structure where in-plane magnetic anisotropy has been reduced significantly, z-axis is no longer magnetic hard axis. In other word, magnetic anisotropy energy for in-plane and out-of-plane has become comparable, despite the fact that still magnetic easy axis is preferable toward in-plane.



 Suspended
  Unsuspended

Figure 5.11 Longitudinal (top) and transverse (bottom) Hall resistance as a function of applied field (R_{xx} vs. H , R_{xy} vs. H) at the temperature of 4 K.



 Suspended  Unsuspended

Figure 5.12 Angle-dependent longitudinal resistance of GaMnAs structure.

5.7 Estimation of anisotropy constant

From the transverse planar Hall response, the ratio of the uniaxial anisotropy constant and the cubic anisotropy can be estimated. In order to estimate this ratio, the data from 15 K with $H = 12000$ Oe was taken. Under the applied magnetic field much greater than the coercive field H_C , the magnetization of the structure rotate simultaneously as the orientation of the magnetic field rotates. As a result, transverse planar Hall resistance satisfies the following relation:

$$R_{xy}(\propto E_y) \propto \frac{k}{t} M^2 \sin 2\theta_M$$

(5.7.1).

Thus, by fitting transverse planar Hall response into Eq. (5.7.1), the magnetization angle θ_M for each applied field angle θ can be deduced. Figure 5.13 illustrate the estimated magnetization angle vs. applied magnetic field angle. If magnetization is always identical to the applied field direction, figure 5.13 must appear in a straight line. However, due to the energy barriers due to magnetic anisotropy, there is magnetization phase lag. Figure 5.14 illustrate the sine value of this magnetization phase lag ($\theta_M - \theta$) as a function of magnetization angle θ_M . Then, figure 5.14 with non-linear function fitting with least square method, one can deduce the value of $\frac{K_U}{M}$ and $\frac{K_C}{M}$ from following fitting function:

$$K_U/M \sin 2\theta_M + K_C/M \sin 4\theta_M + H \sin(\theta_M - \theta) = 0$$

(5.7.2).

Figure 3.15 shows the estimated value of $\frac{K_U}{M}$, $\frac{K_C}{M}$, and $\frac{K_C}{K_U}$. It is clearly shown that relaxation of the local strain in the GaMnAs structure reduced in-plane cubic anisotropy energy so that the ratio $\frac{K_C}{K_U}$ is reduced from 85 to 65 which is ~ 24% reduction.

It is notable that the 24% reduction in ratio $\frac{K_C}{K_U}$ is the result of the local strain relaxation. From the lattice constant estimated from HR-XRD, the compressive strain applied to the GaMnAs with Mn composition of ~6% is less than 0.2%. In other words, relaxation of 0.2% of strain has result about 24% reduction in magnetic anisotropy. This gigantic response in magnetic anisotropy in strain relaxation can be attributed to strong spin-orbit interaction of GaMnAs.

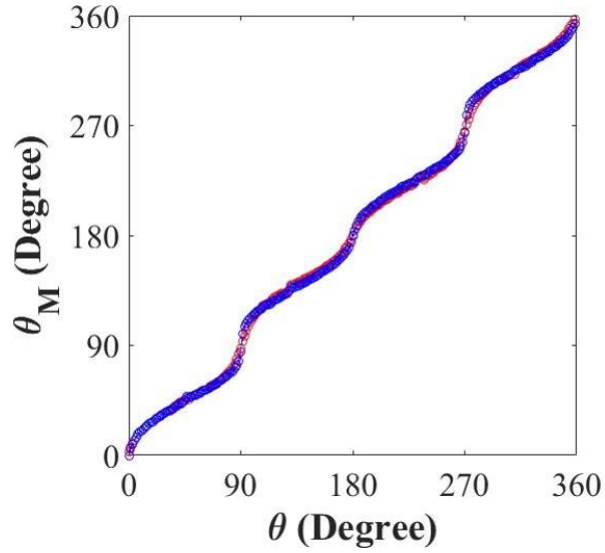


Figure 5.13 Magnetization angle as a function of applied magnetic field angle for (red) suspended and (blue) unsuspended.

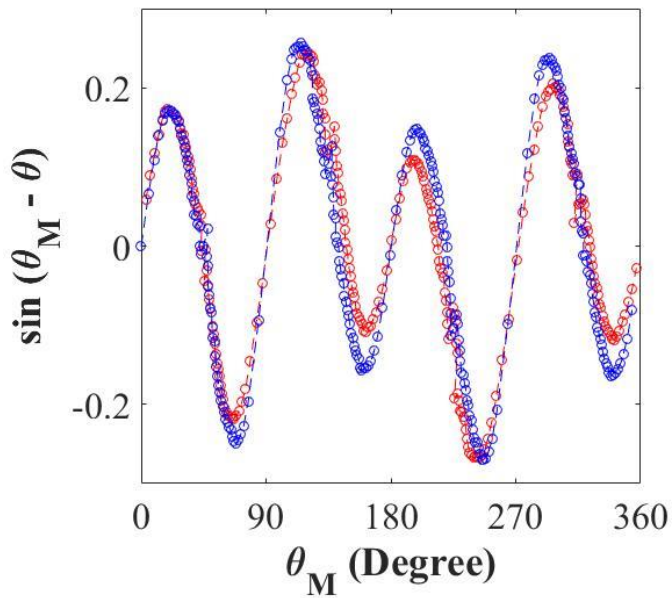


Figure 5.14 Sine value of magnetization phase lag as a function of magnetization angle for (red) suspended and (blue) unsuspended.

	K_U/M	K_C/M	K_C/K_U
Freely-suspended	49	3200	65
Control	40	3400	85

Figure 5.15 Estimated value of $\frac{K_U}{M}$, $\frac{K_C}{M}$, and $\frac{K_C}{K_U}$.

6 Conclusion and Prospect

Anomalous Hall effect in GaMnAs, a typical carrier-mediated ferromagnetic III-V diluted magnetic semiconductor (DMS), have provided an opportunity for additional functionality in semiconductor system. Although origin of this anomalous Hall effects still remain controversial, the mechanism of these effects is widely accepted to be consequence of spin-orbit interaction which is greatly influenced by strain.

Despite the importance of strain in spin-orbit interaction system, manipulation of strain in thin film has been greatly limited by lattice-constant-mismatch and consequential defect/dislocation occurrence. Although recent studies have been developed a few methods for strain manipulation, these methods are mostly based on substrate-wise manipulation and thus can not be free from crack occurrence in the substrate. Furthermore, possible curvature in the structure (buckling) or substrate (bending) may bring averaging effect of multiple magnetic domain with different magnetization angle which prevent application of Stoner-Wohlfarth model.

We have systematically overcome the obstacle from buckling which is the result of lattice mismatch between GaMnAs layer and sacrificial layer by incorporation metallic electric leads. With all GaMnAs/GaAs underneath metallic leads are removed completely, we have isolated GaMnAs structure from its environment (substrate) and relaxed strain within the structure which is built during pseudomorphic growth. Isolated GaMnAs structure shows relaxation of built-in strain which is attributed to the strain 'buffer zone' effect from soft metallic leads.

Magnetotransport measurements were conducted for both freely-suspended and unsuspended GaMnAs structures. Temperature-dependent resistivity measurements confirmed that fabrication process including several lithography and etching process did not modify or alter the macroscopic characteristics of GaMnAs layer. Non-contact optical profiler measurements as well as finite-element-analysis confirmed no significant deformation was occurred during fabrication process and during cryogenic cycle. From longitudinal and transverse Hall effect from suspended structure, we have confirmed that in-plane magnetic anisotropy has been significantly reduced by relaxing the strain in the structure. At the same time, in-plane magnetic anisotropy in the strain-relaxed structure no longer shows domination over out-of-plane magnetic anisotropy. From non-linear fitting, the relaxation of the strain in GaMnAs with strain of $\sim 0.2\%$ reduced the ratio between cubic anisotropy constant and uniaxial anisotropy constant by $\sim 24\%$. Furthermore, magnetic behavior of suspended GaMnAs layer suggest that unstrained GaMnAs has no significant magnetic easy axis: easy axis still lies in-plane, but as dominant as strained (as-grown) structure.

Nano-machined structure we have developed for relaxation of strain without significant deformation can be employed for wide-range of strain manipulation. Since this structure efficiently evade possible occurrence of deformation due to lattice-mismatch, this structure provides a novel method which can act as a foundation for dynamic strain-manipulation which dynamically controls strain of the structure within a single sample. Furthermore, with further device engineering, electrostatic gates could be incorporated, which may be used to actuate

the buckling process. Controlled buckling would evolve in the means to dynamically vary the strain on the GaMnAs, possibly allowing for a GaMnAs bit based on mechanical states.

Energy dissipation has been critical issues in information storage device. Especially, as dimension of device decreases, electric or magnetic static energy dissipated during transition between states are expected to be increased exponentially. On the contrary, increase in energy dissipation during mechanical state transition is significantly small compare to transition between electric or magnetic states. Thus mechanical-state-based information storage device based on dynamic strain-manipulation may open an era of next-generation information storage device.

(Blank page)

Bibliography

- [1] M. N. Baibich *et al.*, Giant Magnetoresistance of (001)Fe/(001)Cr Magnetic Superlattices, *Phys. Rev. Lett.* **61**, 2472-2475 (1988).
- [2] M. Julliere, Tunneling between ferromagnetic films, *Phys. Lett. A* **54**, 225-226 (1975).
- [3] Y. Zhang *et al.*, in *2014 Design, Automation & Test in Europe Conference & Exhibition (DATE)*, 1-6.
- [4] V. A. Dediu *et al.*, Spin routes in organic semiconductors, *Nat. Mater.* **8**, 707-716 (2009).
- [5] S. Datta & B. Das. Electronic analog of the electro-optic modulator, *Appl. Phys. Lett.* **56**, 665-667 (1990).
- [6] D. D. Awschalom *et al.*, *Semiconductor Spintronics and Quantum Computation* (Springer-Verlag Berlin Heidelberg New York, 2002).
- [7] Y. D. Park *et al.*, A Group-IV Ferromagnetic Semiconductor: $\text{Mn}_x\text{Ge}_{1-x}$, *Science* **295**, 651-654 (2002).
- [8] H. Saito *et al.*, Room-Temperature Ferromagnetism in a II-VI Diluted Magnetic Semiconductor $\text{Zn}_{1-x}\text{Cr}_x\text{Te}$, *Phys. Rev. Lett.* **90**, 207202 (2003).
- [9] T. Jungwirth *et al.*, Theory of ferromagnetic (III,Mn)V semiconductors, *Rev. Mod. Phys.* **78**, 809-864 (2006).
- [10] S. J. Pearton *et al.*, Wide band gap ferromagnetic semiconductors and oxides, *J. Appl. Phys.* **93**, 1-13 (2002).

- [11] M. I. Nathan *et al.*, Electron mobility in *p*-type GaAs, *Appl. Phys. Lett.* **52**, 654-656 (1988).
- [12] S. A. Dayeh *et al.*, High Electron Mobility InAs Nanowire Field-Effect Transistors, *Small* **3**, 326-332 (2007).
- [13] D. L. Smith, *Thin-film Deposition* (McGraw-Hill Book Co., 1997).
- [14] G. H. Li *et al.*, Initial Growth of Single-Crystalline Nanowires: From 3D Nucleation to 2D Growth, *Nanoscale Res. Lett.* **5**, 1057-1062 (2010).
- [15] H. Wang *et al.*, Atomistics of vapour–liquid–solid nanowire growth, *Nat. Comm.* **4**, 1956 (2013).
- [16] S. S. A. Seo *et al.*, Ferroelectricity in Artificial Bicolor Oxide Superlattices, *Adv. Mater.* **19**, 2460-2464 (2007).
- [17] T. Cheiwchanchamnangij *et al.*, Strain effects on the spin-orbit-induced band structure splittings in monolayer MoS₂ and graphene, *Phys. Rev. B* **88**, 155404 (2013).
- [18] Y. Liu *et al.*, Tuning Dirac states by strain in the topological insulator Bi₂Se₃, *Nat. Phys.* **10**, 294-299 (2014).
- [19] N. Levy *et al.*, Strain-Induced Pseudo–Magnetic Fields Greater Than 300 Tesla in Graphene Nanobubbles, *Science* **30**, 544-547 (2010).
- [20] G. S. Diniz *et al.*, Engineering the quantum anomalous Hall effect in graphene with uniaxial strains, *J. Appl. Phys.* **114**, 243701 (2013).
- [21] W. Ya-ping *et al.*, Tunable quantum spin Hall effect via strain in two-dimensional arsenene monolayer, *J. Phys. D: Appl. Phys.* **49**, 055305 (2016).

- [22] F. Matsukura *et al.*, Magnetotransport properties of metallic (Ga,Mn)As films with compressive and tensile strain, *Physica E* **21**, 1032-1036 (2004).
- [23] C. Bihler *et al.*, Ga_{1-x}Mn_xAs/piezoelectric actuator hybrids: A model system for magnetoelastic magnetization manipulation, *Phys. Rev. B* **78**, 045203 (2008).
- [24] J. Wenisch *et al.*, Control of Magnetic Anisotropy in (Ga, Mn)As by Lithography-Induced Strain Relaxation, *Phys. Rev. Lett.* **99**, 077201 (2007).
- [25] I. Chasiotis *et al.*, Young's Modulus, Poisson's Ratio, and Nanoscale Deformation Fields of MEMS Materials, *MRS Proceedings*, 795 (2003).
- [26] T. Jungwirth *et al.*, Anomalous Hall Effect in Ferromagnetic Semiconductors, *Phys. Rev. Lett.* **88**, 207208 (2002).
- [27] S. H. Chun *et al.*, Interplay between Carrier and Impurity Concentrations in Annealed Ga_{1-x}Mn_xAs: Intrinsic Anomalous Hall Effect, *Phys. Rev. Lett.* **98**, 026601 (2007).
- [28] H. K. Choi *et al.*, Evidence of metallic clustering in annealed Ga_{1-x}Mn_xAs from atypical scaling behavior of the anomalous Hall coefficient, *Appl. Phys. Lett.* **89**, 102503 (2006).
- [29] M. Matsuo *et al.*, Effects of mechanical rotation and vibration on spin currents, *J. Korean Phys. Soc.* **62**, 1404-1409 (2013).
- [30] P. Mahadevan & A. Zunger, First-principles investigation of the assumptions underlying model-Hamiltonian approaches to ferromagnetism of 3d impurities in III-V semiconductors, *Phys. Rev. B* **69**, 115211 (2004).

- [31] A. H. MacDonald *et al.*, Ferromagnetic semiconductors: moving beyond (Ga,Mn)As, *Nat. Mater.* **4**, 195-202 (2005).
- [32] W. Thomson, On the Electro-Dynamic Qualities of Metals:--Effects of Magnetization on the Electric Conductivity of Nickel and of Iron, *Proc. R. Soc. A* **8**, 546-550 (1856).
- [33] E. M. Lifshits & A. M. Kosevich, Theory of the Shubnikov—de Haas effect, *J. Phys. Chem. Solids* **4**, 1-10 (1958).
- [34] A. B. Pippard, *Magnetoresistance in Metals* (Cambridge University Press, 1989).
- [35] R. V. Coleman & A. Isin, Magnetoresistance in Iron Single Crystals, *J. Appl. Phys.* **37**, 1028-1029 (1966).
- [36] S. N. Sahu *et al.*, *Nano-scale Materials: From Science to Technology* (Nova Science Publishers, 2006).
- [37] H. Gu *et al.*, An overview of the magnetoresistance phenomenon in molecular systems, *Chem. Soc. Rev.* **42**, 5907-5943 (2013).
- [38] K. Rätzke *et al.*, Evolution of microstructure and magnetoresistance in Co/Cu multilayers during annealing, *J. Magn. Magn. Mater.* **204**, 61-67 (1999).
- [39] A. W. Rushforth *et al.*, Anisotropic Magnetoresistance Components in (Ga,Mn)As, *Phys. Rev. Lett.* **99**, 147207 (2007).
- [40] W. Döring, Die Abhängigkeit des Widerstandes von Nickelkristallen von der Richtung der spontanen Magnetisierung, *Annalen der Physik* **424**, 259-276 (1938).

- [41] K. Y. Wang *et al.*, Anisotropic magnetoresistance and magnetic anisotropy in high-quality (Ga,Mn)As films, *Phys. Rev. B* **72**, 085201 (2005).
- [42] C. Chien, *The Hall Effect and Its Applications* (Springer US, 2013).
- [43] E. M. Pugh, Hall Effect and the Magnetic Properties of Some Ferromagnetic Materials, *Phys. Rev.* **36**, 1503-1511 (1930).
- [44] E. M. Pugh & T. W. Lippert, Hall e.m.f. and Intensity of Magnetization, *Phys. Rev.* **42**, 709-713 (1932).
- [45] A. W. Smith & R. W. Sears, The Hall Effect in Permalloy, *Phys. Rev.* **34**, 1466-1473 (1929).
- [46] R. Karplus & J. M. Luttinger, Hall Effect in Ferromagnetics, *Phys. Rev.* **95**, 1154-1160 (1954).
- [47] D. J. Thouless *et al.*, Quantized Hall Conductance in a Two-Dimensional Periodic Potential, *Phys. Rev. Lett.* **49**, 405-408 (1982).
- [48] M.-C. Chang & Q. Niu, Berry phase, hyperorbits, and the Hofstadter spectrum: Semiclassical dynamics in magnetic Bloch bands, *Phys. Rev. B* **53**, 7010-7023 (1996).
- [49] G. Sundaram & Q. Niu, Wave-packet dynamics in slowly perturbed crystals: Gradient corrections and Berry-phase effects, *Phys. Rev. B* **59**, 14915-14925 (1999).
- [50] J. Smit, The spontaneous hall effect in ferromagnetics II, *Physica* **24**, 39-51 (1958).
- [51] J. Smit, The spontaneous hall effect in ferromagnetics I, *Physica* **21**, 877-887 (1955).

- [52] L. Berger, Influence of spin-orbit interaction on the transport processes in ferromagnetic nickel alloys, in the presence of a degeneracy of the 3d band, *Physica* **30**, 1141-1159 (1964).
- [53] L. Berger, Side-Jump Mechanism for the Hall Effect of Ferromagnets, *Phys. Rev. B* **2**, 4559-4566 (1970).
- [54] N. Nagaosa *et al.*, Anomalous Hall effect, *Rev. Mod. Phys.* **82**, 1539-1592 (2010).
- [55] H. Weng *et al.*, Quantum anomalous Hall effect and related topological electronic states, *Adv. Phys.* **64**, 227-282 (2015).
- [56] E. C. Stoner & E. P. Wohlfarth, A Mechanism of Magnetic Hysteresis in Heterogeneous Alloys, *Phil. Trans. R. Soc. A* **240**, 599 (1948).
- [57] L. D. Landau & E. M. Lifshitz, in *Electrodynamics of Continuous Media (Second Edition Revised and Enlarged)* Vol. 8, 130-179 (Pergamon, 1984).
- [58] N. A. Spaldin, *Magnetic Materials: Fundamentals and Applications*, (Cambridge University Press, 2003).
- [59] R. C. O'Handley, *Modern Magnetic Materials: Principles and Applications*, (Wiley, 1999).
- [60] Y. Sun *et al.*, Physics of strain effects in semiconductors and metal-oxide-semiconductor field-effect transistors, *J. Appl. Phys.* **101**, 104503 (2007).
- [61] H. Asai *et al.*, Energy band-gap shift with elastic strain in $\text{Ga}_x\text{In}_{1-x}\text{P}$ epitaxial layers on (001) GaAs, *J. Appl. Phys.* **54**, 2052 (1983).

- [62] S. C. Jain *et al.*, Stresses and strains in epilayers, stripes and quantum structures of III - V compound semiconductors, *Semicond. Sci. and Technol.* **11**, 641 (1996).
- [63] M. Abolfath *et al.*, Theory of magnetic anisotropy in $\text{III}_{1-x}\text{Mn}_x\text{V}$ ferromagnets, *Phys. Rev. B* **63**, 054418 (2001).
- [64] U. Welp *et al.*, Magnetic Domain Structure and Magnetic Anisotropy in $\text{Ga}_{1-x}\text{Mn}_x\text{As}$, *Phys. Rev. Lett.* **90**, 167206 (2003).
- [65] H. Ohno *et al.*, (Ga,Mn)As: A new diluted magnetic semiconductor based on GaAs, *Appl. Phys. Lett.* **69**, 363-365 (1996).
- [66] J. P. Pan, *Solid State Physics* (Academic, 1957).
- [67] K. Pappert *et al.*, Detailed transport investigation of the magnetic anisotropy of (Ga,Mn)As, *New J. Phys.* **9**, 354 (2007).
- [68] J. R. Arthur, Molecular beam epitaxy, *Surf. Sci.* **500**, 189-217 (2002).
- [69] M. Ohring, *Materials Science of Thin Films (Second Edition)* (Academic Press, 2002).
- [70] D. Zhou & B. F. Usher. Deviation of the AlGaAs lattice constant from Vegard's law, *J. Phys. D: Appl. Phys.* **34**, 1461 (2001).
- [71] D. W. Koh *et al.*, Effects of the V/III flux ratio on the Curie temperature of GaMnAs, *J. Korean Phys. Soc.* **45**, 465-469 (2004).
- [72] J.-H. Lee *et al.*, Free-Standing GaMnAs Nanomachined Sheets for van der Pauw Magnetotransport Measurements, *Micromachines* **7**, 223 (2016).
- [73] H. Ohno. Properties of ferromagnetic III–V semiconductors, *J. Magn. Magn. Mater.* **200**, 110-129 (1999).

- [74] H. Ohno, Making Nonmagnetic Semiconductors Ferromagnetic, *Science* **281**, 951 (1998).
- [75] K. W. Edmonds *et al.*, Mn Interstitial Diffusion in (Ga, Mn)As, *Phys. Rev. Lett.* **92**, 037201 (2004).
- [76] G. C. DeSalvo *et al.*, Etch Rates and Selectivities of Citric Acid/Hydrogen Peroxide on GaAs , $\text{Al}_{0.3}\text{Ga}_{0.7}\text{As}$, $\text{In}_{0.2}\text{Ga}_{0.8}\text{As}$, $\text{In}_{0.53}\text{Ga}_{0.47}\text{As}$, $\text{In}_{0.52}\text{Al}_{0.48}\text{As}$, and InP, *J. Electrochem. Soc.* **139**, 831-835 (1992).
- [77] P. Kumar *et al.*, Sacrificial etching of $\text{Al}_x\text{Ga}_{1-x}\text{As}$ for III–V MEMS surface micromachining, *Appl. Phys. A* **88**, 711-714 (2007).
- [78] G. A. Horridge & S. L. Tamm, Critical Point Drying for Scanning Electron Microscopic Study of Ciliary Motion, *Science* **163**, 817 (1969).
- [79] T. Jungwirth *et al.*, Dc-transport properties of ferromagnetic (Ga,Mn)As semiconductors, *Appl. Phys. Lett.* **83**, 320-322 (2003).
- [80] O. Shinya *et al.*, Strain-induced reversible modulation of the magnetic anisotropy in perpendicularly magnetized metals deposited on a flexible substrate, *Appl. Phys. Express* **9**, 043004 (2016).
- [81] H. X. Tang *et al.*, Giant Planar Hall Effect in Epitaxial (Ga,Mn)As Devices, *Phys. Rev. Lett.* **90**, 107201 (2003).

국문 초록

이 논문은 강자성의 뭉은 자성 반도체인 GaMnAs 를 자가 현수시킨 구조물에서의 anomalous Hall 효과와 planar Hall 효과에 대한 연구를 담고 있다. GaMnAs 는 정공에 의해 매개되는 강자성을 가지는 반도체로 특히 스핀-궤도 상호작용이 강한 물질이다. 응집 물질 물리계에서 유일한 상대론적 효과인 스핀-궤도 상호작용이 강한 물질의 경우 전자 밴드 구조를 직접적으로 변화시키는 역학적 변형에 의한 효과가 매우 크게 나타난다.. 특히, GaMnAs 의 경우 분자선 켜쌓기 방식으로 성장하는 과정에서 역학적 변형을 지니고 있을 수 밖에 없고 이러한 역학적 변형의 방향에 따라 그 자화의 방향이 in-plane 이나 out-of-plane 방향으로 정렬되려는 성질을 지니고 있다. 이러한 개념을 바탕으로 많은 연구진들은 GaMnAs 의 역학적 변형을 통해 그 자기적 성질을 변화하고자 노력해온 바 있다 하지만 기존의 방법의 경우 GaMnAs 아래에 성장시키는 물질에 변화를 주는 정적인 방식이 주를 이루고 동적인 방식 역시 기판 전체를 휘거나 압전 소자를 활용하여 기판을 당기는 방식이기에 변경할 수 있는 역학적 변형의 크기와 방향에 그 제약을 받게 된다. 따라서 본 연구에서는 나노 구조 제작 기술을 활용하여 이미 성장된 GaMnAs 상의 역학적 변형을 제거하고 나아가

역학적 변형이 없는 자유로운 상태의 GaMnAs 자기적 성질을 밝히고자 하였다.

우선 저온 분자선 켜쌓기 방식을 통해 GaMnAs 를 AlGaAs 위에 성장시킴으로써 약 0.2% 의 역학적 변형을 지닌 GaMnAs 를 성장시켰다. 성장시킨 GaMnAs 를 전자빔 리소그래피 기술과 여러가지 식각 기술을 활용하여 외부로부터 독립된 GaMnAs 구조를 자가 현수 시켰다. 자가 현수된 구조물의 경우 부드러운 금속 전극으로 외부와 연결되어 있기에 성장과정에서 생긴 역학적 변형을 금속 전극이 완충함으로써 역학적 변형을 해소할 수 있었다. Finite element analysis 방식을 통해 상온에서 저온까지 이러한 역학적 변형의 해소를 수치적으로 확인하였다. 또한 이렇게 제작된 GaMnAs 구조물을 극저온 환경에서의 자기 저항을 측정함으로써 자기 이방성의 변화를 확인하고자 하였다.

자기 이방성을 측정하기 위하여 극저온에서 (~ 4 K) 강한 자기장을 걸어 (~ 1.2 T) 자가 현수된 GaMnAs 구조와 현수되어 있지 않은 구조에서의 anomalous Hall 효과와 planar Hall 효과를 측정하고 비교한 바 자가현수된 구조의 경우 in-plane 자기 이방성에 의한 자기 저항 효과가 현저하게 줄어드는 것을 확인하였으며 out-of-plane 자기 이방성에 의한 자기 저항 효과는 증가하는 것 또한 확인할 수 있었다. 이러한 자기 이방성 효과의 변화는 결국 자가 현수를 위해 삽입한 부드러운 금속 전극이 성장과정에서 발생한 역학적 변형을 해소했다는 것을 의미한다. 이를 통해 역학적 변형을 정적인 방식이나 기판 전체를

변형하는 방식이 아닌 국소적인 역학적 변형을 나노 구조 제작 기술을 통해 달성할 수 있음을 제시하였다. 이와 더불어 수정된 Stoner-Wohlfarth 모델로의 fitting 을 통해 in-plane biaxial cubic 자기 이방성과 in-plane uniaxial 자기 이방성의 비를 약 24% 정도 낮추었음을 확인하였다. 이는 약 0.2% 미만의 역학적 변형을 해소함으로써 얻은 결과라는 것을 고려해보면 역학적 변형은 스핀-궤도 상호작용 기반의 물리 현상을 변화시키는 매우 강력한 파라미터임을 알 수 있다. 이와 더불어 기존의 완충층이나 희생층이 아닌 나노 구조 제조 기술을 기반으로 하는 역학적 변형의 해소가기에 나아가 동적인 역학적 변형 제어로 나아갈 수 있을 것으로 기대되는 바이다.

핵심 단어 : 물은 자성 반도체, GaMnAs, 분자선 켜쌓기, 자기 현수, 자기 저항, 비정상 홀 효과, 평면 홀 효과, 자기 이방성, 역학적 변형

학 번 : 2008-20446